Universiteit
Leiden
The Netherlands

Squaramide-based interpenetrated networks for load-bearing applications

Chen, Y.

Citation
Chen, Y. (2024, November 8). *Squaramide-based interpenetrated networks for load-bearing applications*. Retrieved from https://hdl.handle.net/1887/4108020

Version:	Publisher's Version
License:	Licence agreement concerning inclusion of doctoral thesis in the Institutional Repository of the University of Leiden
Downloaded from:	https://hdl.handle.net/1887/4108020

Note: To cite this publication please use the final published version (if applicable).

Chapter 4

Visible Light Crosslinking of Hybrid Covalent and Supramolecular Double Networks for Dynamic Mechanical Loading of 3D Chondrocyte Cultures

Double network hydrogels are highly suitable for applications in 3D platforms for articular cartilage engineering because of their excellent mechanical properties and structural features that are comparable to the *in vivo* extracellular matrix. However, employing synthetic hydrogels to closely mimic the mechanical responses that occur in the tissue under cyclic compressive loading conditions remains challenging. Herein, we explore phenol photopolymerization with visible light to connect filamentous supramolecular and covalent networks to give rise to a double network hydrogel. Modulation of the crosslinking density led to changes in the complex mechanical characteristics of the double network hydrogels. Furthermore, biomimetic compression stress responses can be modulated by tuning component ratios. These hydrogels also exhibited fast stress relaxation in both shear and axial directions, with the relaxation rate mainly dependent on the supramolecular polymer concentration and crosslinking density. Crosslinking of the two networks permitted cyclic compressive loading of human primary articular chondrocyte cultures in 3D showing increased sulfated-glycosaminoglycan deposition relative to the free swelling condition after 2 days. Utilizing rapid visible light-induced bioorthogonal photopolymerization, this innovative approach enables the fabrication of double network hydrogels with customizable biomimetic mechanical characteristics by strategically adjusting chemical design parameters that is crucial for joint regeneration and can be used to develop advanced materials tailored for 3D *in vitro* modeling of cartilage and targeted therapeutic interventions for osteoarthritis.

This chapter was prepared as a research article: Ying Chen, Yolande Ramos[*]& and Roxanne E. Kieltyka[*]

4.1 Introduction

Articular cartilage is a remarkable natural material that can endure high contact pressures for human daily activities due to its excellent mechanical properties and low friction.[1,2] It is a biphasic material composed of collagen fibers and proteoglycans (PGs) with glycosaminoglycan (GAG) side chains and synovial fluid that differs in its presentation across cartilage leading to distinct mechanics across the tissue.[1,3-5] An essential part of this matrix is the pericellular matrix (PCM) that is immediately adjacent to the cell membrane and together with the cell forms the chondron. It is composed of fibrous network-like collagens (e.g., types II, VI, and IX), fibronectin, and proteoglycans (e.g., aggrecan, hyaluronan and decorin), transmitting both biophysical and biochemical cues from the tissues to the cells.[6] The PCM exhibits distinct mechanical properties from the surrounding chondrocyte extracellular matrix (ECM), and is altered during development and in disease like osteoarthritis (OA).[6-9] Nowadays, studies show that synthetic hydrogel materials, based on their mechanical properties, can be used to mimic and regenerate PCM with the proper external mechanical stimulus, highlighting the potential of mechanical loading on cartilage constructs *in vitro* to mimic the native environment and stimulate biosynthesis in chondrocytes.[10,11]

In the biphasic cartilage system, the cross-linked collagen fibers act as a first phase that sustains tension, whereas the synovial fluid acts as a second phase that swells yielding pores, which gives rise to the ability to dissipate energy upon loading through combining fluid-solid frictional dissipation with the inherent viscoelasticity of the solid matrix.[3] *In vivo*, cartilage experiences dehydration and rehydration on loading and can bear contact pressures greater than its compressive modulus due to fluid pressurization within its porous structure.[5] The time-dependent properties of cartilage result from the complex interplay between the solid matrix and fluid flow that can be characterized by poroelastic and viscoelastic mechanisms that impart a wide range of dissipative properties.[5] Hereby, poroviscoelastic (PVE) relaxation describes the combination of poroelastic and viscoelastic relaxation that happens simultaneously.[12,13] Poroelastic relaxation originates from stress-induced fluid flow (diffusion), which dissipates energy through fluid-solid frictional interaction, and its time constant depends on a characteristic diffusion length scale.[14,15] Viscoelastic relaxation is the property of a material that can resist deformation under stress due to the rearrangement and interactions of solid matrix macromolecules (i.e., collagen fibrils and PGs).[16-18] Rapid PVE relaxation can govern the rate-dependent mechanical response of intact cartilage and can protect the joints against external forces. To date, few examples consider the combination of these mechanical properties in their design to develop synthetic cartilage ECM mimics, most research focuses either on the poroelastic or viscoelastic property of the material.[19,20]

Double network (**DN**) hydrogels provide an opportunity to mimic the cartilage ECM because of their unique stiff and tough mechanical properties.[21] These hydrogels are composed of two independent networks that are crosslinked with one another, either through physical or chemical interactions,[11, 12] showing improved stiffness, mechanical strength and load-bearing properties that differ significantly from the independent networks.[8-10] However, most **DN** networks lack a fibrous network and dynamic biomimetic mechanics (e.g., viscoelasticity, plasticity, etc.)[22-34] that is found in

the native ECM. Supramolecular filaments are often introduced into **DN** hydrogels to improve stress relaxation because of their energy dissipation properties when subjected to external stimuli.[22,23,35-37] Moreover, most researchers currently concentrate on enhancing mechanical properties by utilizing a single type of chemical bond, the potential influence of chemical bond types and ratios in the synthetic network on stress relaxation in hydrogels has often been overlooked. Therefore, it is vital to develop complex network architectures that modulate these features to understand the range by which such materials can be altered for a given application.[1118,38,39] Light-based cross-linking methods are extensively employed in the preparation of **DN** materials due to their versatility and controlled deployment.[40,41] UV light (200-400 nm) is commonly used due to its high efficiency in initiating photopolymerization reactions.[41-43] Recently, visible light (400-700 nm) has also been widely explored, offering advantages such as reducing photodamage to living cells for biomedical application.[44,45]

We earlier demonstrated the formation of filamentous **DN** hydrogels that show biomimetic mechanical properties that are cartilage-like in their compression using bioorthogonal UV light-mediated polymerization strategy to crosslink supramolecular and covalent polymer networks through dynamic-covalent poly(disulfide) and poly(disulfide-norbornene)s (**Chapter 3**). We used this hybrid **DN** network for 3D cell culture of human primary articular chondrocytes under external cyclic mechanical loads to enhance the deposition of sulfated-glycosaminoglycans. Inspired by these results, we became interested in developing another **DN** hydrogel network based on the formation of covalent polymer crosslinks to further increase the mechanics of the network advancing our progression towards mimicking the properties of native tissues. In this study, we disclose a visible light-induced bioorthogonal strategy involving phenol photopolymerization crosslinking of supramolecular filament and covalent poly(ethylene glycol) networks to develop hybrid networks that are suitable for diurnal cyclic compressive loading of 3D chondrocyte cultures. Phenol crosslinking chemistry is a widely used method in biomaterial field due to its mild and fast crosslinking characteristic, the chemical ligation will permit the formation of networks connected through polyphenol networks with distinct dynamic characters in the **DN** hydrogels. In this **DN** network, we select a 4-arm polyethylene glycol with an additional orthogonal bond in the backbone to further increase the **DN** mechanical strength. Next, we conduct an in-depth examination of the interplay between supramolecular content and poly(ethylene glycol) network concentration, focusing on their impact on the mechanical stiffness, strength, and poroviscoelastic relaxation within the **DN** system. Importantly, we explore the capacity of **DN** hydrogel to endure cyclic compressive loading to assess its mechanical attributes in mimicking the load-bearing tissues that are crucial for investigating a spectrum of inquiries related to both developmental processes and disease-related phenomena.

4.2 Results and Discussion

Visible light crosslinking of hybrid supramolecular and covalent DN hydrogels

To prepare the **DN** hydrogels with light responsive phenols for crosslinking, we introduced phenol moiety (Phe) first on the periphery of the squaramide amphiphile derived from a typical tripodal squaramide-based gelator, C8-SQ[46] (Scheme 1A, Figure S1). We conjugated a tosyl (Ts)-protected

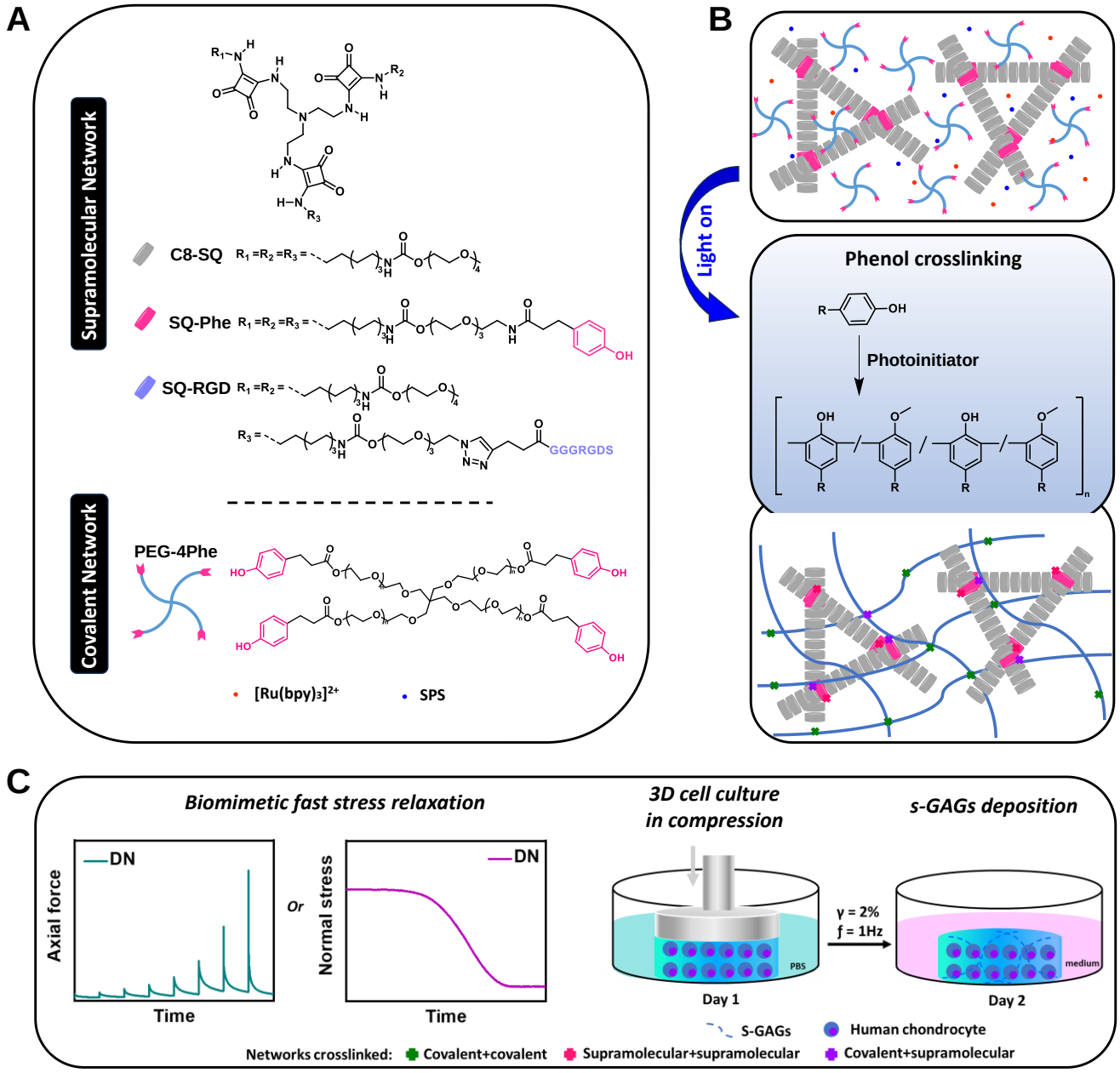

Scheme 1. (A) Supramolecular filament (SN: C8-SQ, SQ-Phe, and SQ-RGD) and covalent polymer (PN: PEG-4Phe) component to prepare **DN** hydrogels. (B) Mixing of components, phenol photopolymerization to form **DN** hydrogels. (C) Biomimetic cartilage mechanical properties can be achieved in compression and release (*left and middle left*). The bioorthogonal photopolymerization approach in the **DN** hydrogel permits 3D human chondrocyte culture with cyclic compression leading to increased s-GAGs deposition (*middle right and right, respectively*).

tetraethylene glycol with an azide and then reduced the azide into amine by catalytic hydrogenation, and further protected the amine with tert-butyloxycarbonyl (Boc). Afterward, we coupled the Boc-protected tetraethylene glycol with carboxybenzyl (Cbz)-protected 1,8-dibromodecane in the presence of sodium hydroxide through a carbamate moiety with a yield of ~33%. We then deprotected Cbz-protecting group by catalytic hydrogenation to reveal an amine moiety, which was further reacted with dibutyl squarate to yield the squaramide amphiphile in ~56%. Furthermore, we connected the squaramide amphiphile onto the tris(2-aminoethylamine) (TREN) core to obtain Boc-protected tripodal squaramide-based monomers in a yield of ~43%. In a final step, we used trifluoroacetic acid (TFA) to deprotect the Boc-protected amine group on the periphery of the tripodal amphiphile and coupled 3-(4-(tert-butoxy)phenyl)propanoic acid, and then deprotected the tert-butyl group by TFA to obtain the final phenol functionalized tripodal squaramide-based monomers (SQ-Phe) in a yield of ~43%. C8-SQ was synthesized as we reported before.[47] Subsequently, we introduced phenol on the 4-arm polyethylene glycol (Mn = 10 kDa) by using carbodiimide coupling chemistry, and deprotected by TFA to obtain a high degree of functionalization of PEG-4Phe as earlier reported.[48,49]

We prepared the **DN** hydrogels by co-assembling the tripodal squaramide-based supramolecular polymers with 5 mol% phenol (Phe) monomer (2-6 mM) (**SN**) and PEG-4Phe (PN, 1-2% wt%). More precisely, we incorporated the PEG-4Phe polymer into a solution containing supramolecular filaments in phosphate buffered saline (pH 7.4) after sonication on ice, and then brought them to room temperature (RT) overnight to form hydrogels. Subsequently, we added photoinitiator stock solutions of tris(bipyridine) ruthenium (II) chloride (Ru, 44 mM) and sodium persulfate (SPS, 440 mM) before applying visible light at 450 nm to crosslink the soft hydrogels to form **DN**s. The hydrogels remained transparent after photocrosslinking with a yellow colour (Figure S2). In this study, we prepared a series of hydrogels **DN1**-**6** by modulating the concentration of PEG-4Phe and supramolecular networks (Table S1). For **DN1**-**3**, PEG-4Phe concentration remained at 1%, while the concentration of the supramolecular network ranged from 2 mM to 6 mM. For **DN4**-**6**, PEG-4Phe concentration was fixed at 2%, with supramolecular concentration varying from 2 to 6 mM.

Augmentation of the supramolecular network stiffness with addition of the second network

We quantified the impact of combining the covalent network with filamentous supramolecular polymers and phenol photopolymerization on the mechanical characteristics of the **DN1** - **DN6** hydrogels in PBS (pH 7.4) by oscillatory rheology. In time sweep measurements after 3 min visible light irradiation, **DN** hydrogels storage moduli (G') showed greater than the individual components (Figure 1A-B, Table S1). For the single network hydrogels, the polymer network **PN** (1-2 wt%) with Ru (0.05 mM) and SPS (0.5 mM) showed a G' of ~1 kPa -2 kPa, and the supramolecular network **SN** (2-6 mM) reached ~450 Pa – 6.3 kPa (Table S1). For the double network **DN** hydrogels, incorporating the supramolecular **SN** with the covalent **PN** networks yielded G' ranging from ~10 kPa -35 kPa. This increase in storage modulus surpassed the combined values of the **SN** and **PN** individually and markedly exceeded that of the pre-UV exposed hydrogel (~1.5 Pa- 38.2 Pa), underscoring the synergistic effect of integrating these networks and their photocrosslinking. We could further tune the stiffness of these **DN** hydrogels by

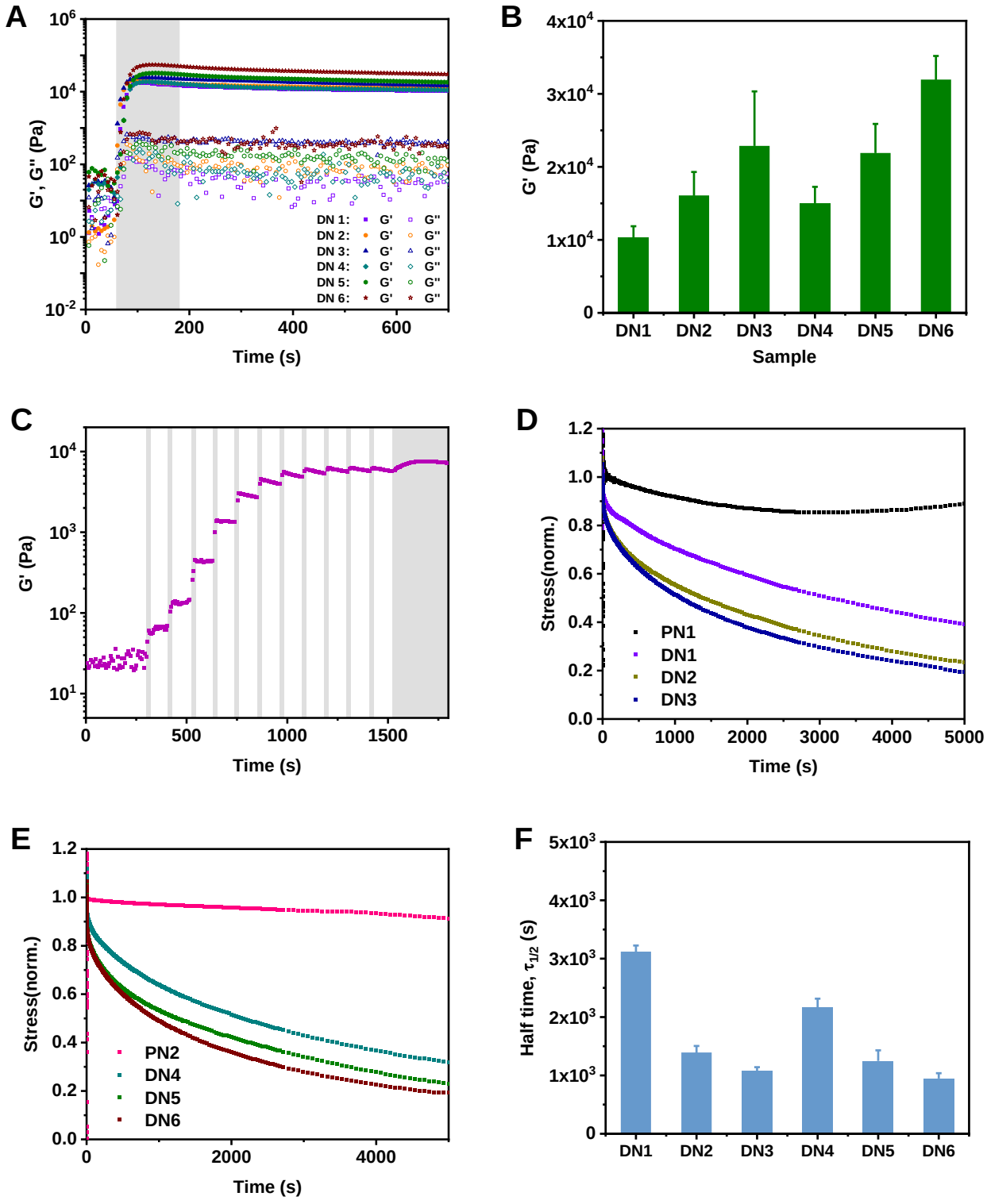

Figure 1. Oscillatory rheology measurements of **DN1-6** hydrogels in PBS at RT: (A) Time sweeps of **DN** hydrogels with 3 min visible light irradiation. (B) Storage modulus (G') at plateau hydrogels with and without 3 min visible light irradiation. (C) Averaged time sweep (N=3) with stepwise UV exposure of the **DN1** hydrogel. (D) Stress relaxation measurements (10% strain) of crosslinked **DN1**-**3** hydrogels. (E) Stress relaxation measurements (10% strain) of crosslinked **DN4**-**6** hydrogels. (F) Stress relaxation half-time of **DN1**-**6** hydrogels. Light source parameters: ~10 mW/cm^2, 400 - 500 nm filter with maximum absorbance at 450 nm. Grey regions indicate visible light exposure. Mean $\pm$ SD, N $\geq$ 3.

modulating the covalent (PEG-4Phe) or supramolecular polymer (SQ-5Phe) concentrations. For example, raising the SQ-5Phe monomer concentration from 2 - 6 mM in the 1 wt% PEG-4Phe networks (**DN1** - **DN3**), the storage modulus of crosslinked **DN** hydrogels grew from ~10 kPa (**DN1**) - ~23 kPa (**DN3**). In contrast, increasing the **PN** concentration to 2 wt%, boosted the storage modulus from 15 kPa (**DN4**) - 32 kPa (**DN6**). These outcomes are likely because due to the mechanism of cross-linking by the phenol group that undergoes photopolymerization with itself on both networks to achieve the stiffnesses of the **DN** material. Furthermore, application of visible light in a step-wise manner, also augmented the storage modulus of **DN1** from the ~20 Pa - ~10 kPa opening possibilities to modulate the network's mechanical properties in time in a user-defined manner (Figure 1C). Strain-dependent oscillatory rheology (ƒ=1Hz, γ=0.01% - 2000%) of photocrosslinked **DN1** - **DN6** hydrogels displayed a broad linear viscoelastic region (LVR) yielding at ~180% strain (Figure S3A). Frequency sweep data within the LVR (strain=0.05%, frequency=0.2 Hz – 1 Hz) of **DN1** - **DN6** hydrogels showed a linear profile with the G' being greater than the loss modulus (G'') across the whole range of frequencies studied (Figure S3B). These results shows that photocrosslinked double networks can be tuned to display stiffness within the range of the PCM of cartilage (40 kPa – 70 kPa)[8] and other soft tissues (10 kPa – 100 kPa).[50]

To understand the contribution of crosslinking both networks to the DN mechanical properties, we prepared a semi-interpenetrating network (**IPN**) with the same concentration as the **DN3** and **DN6** but without 5 mol% SQ-Phe crosslinking composition in the **SN** component that enables crosslinking of both polymers. The lack of crosslinks between both networks yielded storage moduli ranging from ~2.5 kPa – 8.5 kPa, which was higher than that of the **SN** and **PN** individually, yet lower than that of the **DN** hydrogels. These results indicate that physical characteristics of both networks and their chemical crosslinking serve an important role to achieve the **DN** properties.

Alteration of the hydrogel complex mechanical characteristics with visible light

The hydrogel complex mechanical features can impact cell behaviour in processes such as differentiation and morphogenesis, thus we investigated the viscoelastic and viscoplastic properties of **DN1-6** hydrogels in response to shear deformation. The viscoelasticity of the hydrogel can be determined by its stress relaxation response to a constant strain. We found that the stress relaxation process was predominantly contingent upon **SN** concentration rather than their stiffness (Figure 1D-F), contrary to typical trend where stiffer hydrogels show lower stress relaxation rate.[51,52] **DN1** relaxed ~61 % of the initial stress over the measurement time frame, while **DN2** and **DN3** showed a more pronounced relaxation of ~77 % and ~81 %, respectively. We found a similar trend for **DN4** (~68 %), **DN5** (~77 %), and **DN6** (~81 %). These results indicate that the addition of polymer network could not greatly affect the stress relaxation, but **SN** could help to release more stress. Furthermore, while the **DN** hydrogels exhibited heightened stress relaxation as the **PN** content increased from 1 to 2 wt% with a constant **SN** concentration of 2 mM, no significant alteration was observed with increasing **PN** content when **SN** concentrations were 4 mM or 6 mM. We further evaluated the stress relaxation rate of **DN1-6** by its half time ($\tau_{1/2}$), or the time point when stress release to half of the initial value. The curves showed a range from ~3100s to ~947s when tuning the supramolecular filament and polymer

concentration. In contrast, the **PN** hydrogels (**PN1** and **PN2**) exhibited minimal stress relaxation behavior, consistent with their elastic nature. These results emphasize the significance of supramolecular networks as they give rise to the viscoelastic behaviour recorded in these materials. These results further corroborate that the stress relaxation of these **DN**s is decoupled from stiffness and suggests that the fibrous supramolecular network could enhance the stress relaxation mechanism.

We further probed the viscoplastic response of the materials to the application of stress and its release by a creep and recovery test. We recorded subtle differences in plasticity in the recovery phase of the measurement for the different **DN** networks. **DN1** showed a slightly higher degree of plasticity (~14%), in contrast to **DN2** - **DN6** (~2% - 9%) after visible light crosslinking (Figure. S4). Moreover, the strong linear correlation with time for the creep curves (except **DN1**) points to an increased elastic character of the double networks due to the polyphenol crosslinks.

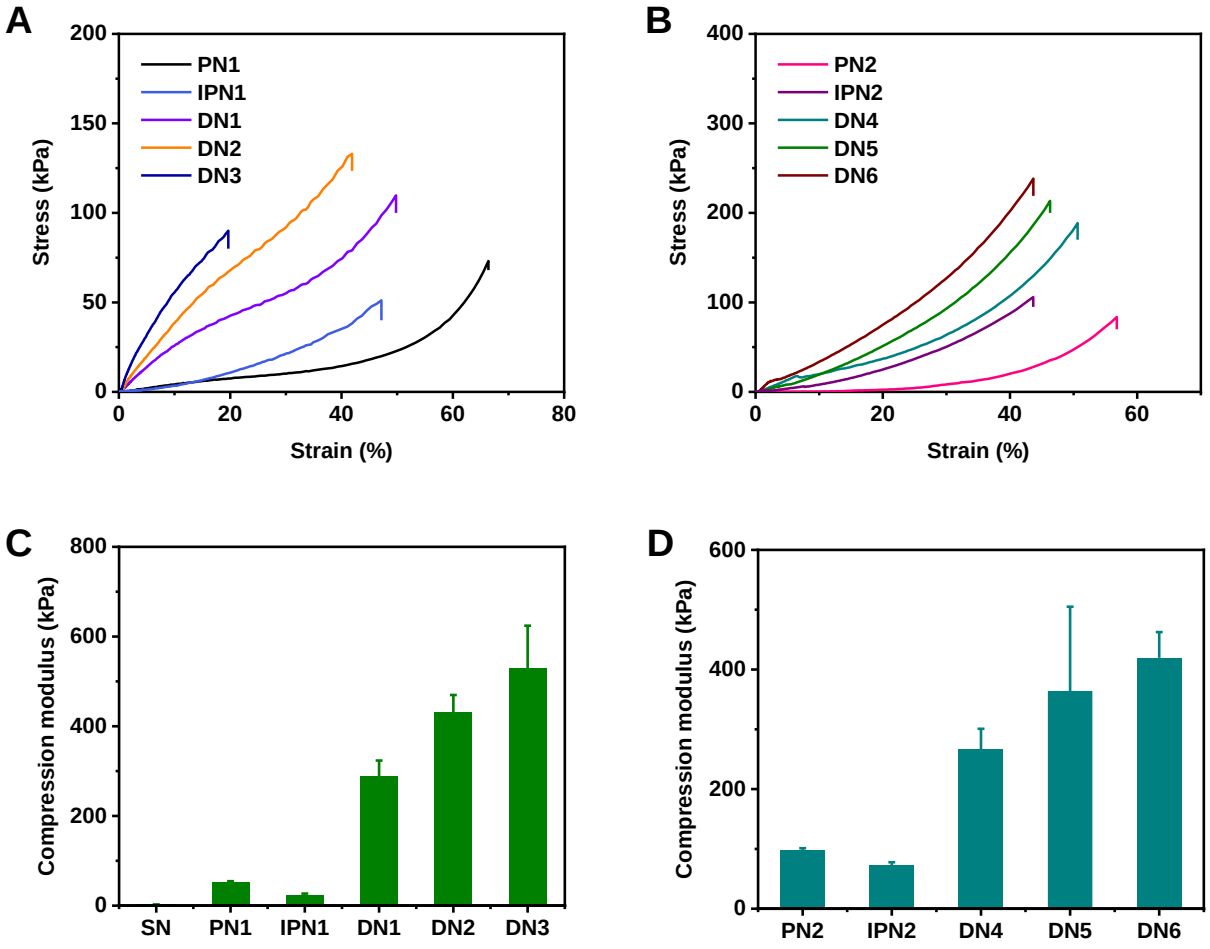

Figure 2. Compressive properties of the **SN**, **PN, IPN,** and **DN** hydrogels under a constant speed of 10 µm/s. Uniaxial stress-strain curves of (A) **PN1**, **IPN1**, and DN1-3 and (B) PN2, IPN2, and **DN4-6**. Compression modulus of (C) **SN**, **PN1**, **IPN1**, and DN1-3 and (D) PN2, IPN2, and **DN4-6**. Mean ± SD, N ≥ 3.

Table 1. Fracture strain, facture stress, fracture energy and compression modulus of **PN**, **IPN** and **DN** hydrogels under 10 µm/s speed, Mean ± SD, N ≥ 3.

Name	Fracture strain (%)	Fracture stress (kPa)	Fracture energy (kJ/m³)	Compression modulus (kPa)
SN	1.44±0.08	7.98±0.91	0.05±0.004	554.94±33.25
PN1	67.61±3.70	58.08±1.97	13.45±4.01	52.58±2.01
IPN1	46.29±1.24	48.05±4.35	9.08±1.12	23.67±2.54
DN1	54.38±3.37	108.44±35.85	43.16±2.12	288.44±35.05
DN2	35.55±3.59	110.88±18.93	18.31±2.65	430.59±39.14
DN3	19.11±6.96	90.03±23.37	9.25±3.24	529.43±94.75
PN2	67.68±1.88	72.93±1.32	23.72±2.22	97.98±3.21
IPN2	44.68±0.92	111.10±7.29	19.39±4.80	71.88±4.84
DN4	49.44±6.14	177.15±39.17	31.76±11.96	266.56±34.28
DN5	44.02±6.18	176.45±61.48	45.30±2.35	364.19±140.72
DN6	47.00±4.72	232.51±8.31	45.22±2.82	419.61±43.00

DN hydrogels withstand compressive loads

The ability to withstand high compressive forces is a defining feature of articular cartilage, therefore understanding the contribution of the supramolecular/polymer concentration, crosslinking type and density to the mechanical properties of the hydrogels is essential.[53] We performed axial force compression tests on the crosslinked **DN1**-**6**, **IPN1-2**, **PN1**-**2** and **SN** hydrogels in the rheometer. The **SN** hydrogel (6 mM) demonstrated brittle behaviour, fracturing at a stress of ~8 kPa (Figure S5). The **PN1**-**2** hydrogels showed high fracture strains (**PN1**: ~68 %, **PN2**: ~65 %), but relatively low fracture stresses (**PN1**: ~58 kPa, **PN2**: ~73 kPa) and fracture energies (**PN1**: ~13 kJ/m^3; **PN2**: ~24 kJ/m^3) (Figure 2A-B, Table 1). The compression curves displayed the typical appearance for polymer materials showing a gradual increase at low strains, followed by a dramatic increase above 45%.

When incorporating 1 wt% **PN** into **SN** to develop **DN1-3**, the resulting hydrogels exhibited greater brittleness with a higher **SN** concentration showing higher fracture stresses, but a lower fracture strain compared to the **PN1** hydrogel (Figure 2A-B, Table 1). Notably, **DN1** exhibited a fracture strain of ~54% with a corresponding fracture stress of ~108 kPa. While **DN3** demonstrated a fracture strain of ~19% along with a fracture stress of ~90 kPa. The fracture energy of **DN1** (~43 kJ/m^3) greatly improved compared with **PN1**, while **DN2** (~18 kJ/m^3) and **DN3** (~9 kJ/m^3) showed a noticeable downward trend. Further increasing the **PN** to 2 wt%, the fracture stress (~177 kPa - 233 kPa) and fracture energy (~32 kJ/m^3 – 45 kJ/m^3) greatly increased compared to **PN2**, and the fracture strain remained relatively constant (~44% - 49%). For comparison, we evaluated the **IPN** hydrogels under identical conditions revealing a fracture stress that is marginally higher than that of **PN** but lower than

that of **DN** (Figure S6), illustrating that the presence of crosslinks between **PN** and **SN** enhances their capacity to withstand stress.

Interestingly, all the **DN** hydrogels showed obvious two-stage compression curves compared with **PN** and **IPN** hydrogels. For **DN1**-**2** hydrogels initially exhibited a linear elastic behavior (< ~25% strain) with a downward concavity, followed by a nonlinear response characterized by an upward concavity until broken. When the supramolecular filament concentration increased in **DN3**, the first stage of the compression curves was prolonged, and **DN3** hydrogels were more brittle with a lower fracture strain and higher fracture stress. The **DN4**-**6** hydrogels exhibited a different trend displaying a slight break at low strain initially (< ~8%, ~23 kPa) in the compression tests, and similar increases with comparable fracture stress. Such behavior is consistent with the theory of linear poroelasticity.[54,55] We hypothesized that the first step primarily results from the supramolecular fibers resisting the stress and acting as a sacrificial network even during the early compression stages. In the second stage polymer network behaviour is observed, resisting most external forces. These findings emphasize the importance of adjusting the amounts of supramolecular fibers and polymer components to achieve a suitable **DN** network for specific applications.

The compression modulus of the **DN1-6** hydrogels grew with the increasing **SN** concentration while maintaining a consistent amount of **PN** (Figure 2C-D, Table 1). In contrast, the extent of this enhancement was slightly reduced as the **PN** concentration increased while maintaining the same **SN** concentration. Furthermore, upon removing the crosslinks between the **PN** and **SN** in the **IPN**, a slight increase in compressive modulus compared to the **PN** was observed, highlighting that the entangled supramolecular filaments could reinforce networks. These findings suggest that there is a synergy between the supramolecular and polymer components on the double network mechanical properties.

An important mechanical feature of cartilage is its poroelasticity that gives rise to its excellent functional performance in load bearing and lubrication. This characteristic encompasses fluid pressure and viscous flow within the ECM, playing an essential role in load-bearing, energy dissipation, solute and fluid transport and mechanotransduction.[56,57] To examine poroelasticity of the **DN**s and **PN**s, we evaluated the effect of loading speed on the **DN** and **PN** compressive properties. We reported a mildly higher compression moduli for **DN** hydrogels (Figure S7-13) deformed at a fast-loading speed of 100 µm/s as compared to 10 µm/s, whereas compression speeds below 10 µm/s resulted in much lower moduli but higher fracture strengths. For example, the fracture strain, stress and energy of **DN6** gel stayed relatively similar when the compression speed decreased from 100 µm/s to 10 µm/s. However, these parameters significantly increased with further reductions in speed. The augmented fracture strength of **DN6** at lower speeds indicates the influence of external stimuli on mechanical strength. At reduced speeds, polymer chains are given sufficient time to respond and endure external forces, thereby enhancing fracture strength. A similar trend was observed for **DN3** and **DN5**. However, the **DN1-2** and **DN4** showed the highest fracture strength at 1 µm/s, demonstrating that the mechanical compressive characters were shared impact of both network composition and external stimulus. These results suggest that the composite material can be optimized to emulate human daily activities that involve varying frequencies.

The supramolecular network enables compressive stress relaxation properties in DN hydrogels

A characteristic feature of cartilage is its ability to rapidly release the stress generated from compressive loads as a joint protection mechanism.[23,39,58] We measured the capacity of the **DN**s to relax successive compressive loads by rapidly applying an increase in strain over 600s in a stepwise manner. The **DN** hydrogels efficiently and instantaneously relaxed the imposed stress (> 85%) in a similar manner to cartilage (Figure 3A-B). The **PN** and **IPN** hydrogels also showed this response profile by relaxing the applied stress (> 80%) to a similar extent as the **DN** under identical conditions but with a reduced axial force response at the start of the load cycle (Figure S15-16). We further measured the capacity of these materials to dissipate energy with increasing cyclic strains to gain further insight into the contribution of the supramolecular network on this property. The hysteresis loops of the **DN** hydrogels expanded on elevating the strain or **SN** concentration (Figure 3C-D, S7-12, S14-15), and the **IPN** and **PN** hydrogels showed reduced dissipated energies in contrast to the **DN** hydrogels. These results highlight that the combination of both covalent and supramolecular networks and their crosslinking are needed to gain access to and maximize these mechanical responses.

Poroviscorelaxation behavior is a distinctive characteristic of articular cartilage's mechanical properties. The reorganization of the network due to external forces can impact liquid transport, potentially affecting biosignal transportation in native tissues.[12,59-62] We then examined the poroviscorelaxation behavior of hydrogels under a consistent normal strain (∼1s) while monitoring their ability to alleviate stress over time. **DN1-6** hydrogels exhibited a quick stress relaxation process, while **PN1-2** and **IPN1-2** hydrogels showed a slower process at the same time scale under a constant strain at 15% (Figure 3E-F, S14-15). Moreover, all the hydrogels exhibited two distinct fast relaxation processes at similar time scales (τ_1 and τ_2). Illustratively, the complete stress dissipation of **DN6** hydrogel required ∼1000s when subjected to a 15% strain. In contrast, both the **PN2** and **IPN2** hydrogels necessitated a more extended duration of 2000s to fully alleviate stress under identical conditions, illustrating that the supramolecular network and the polymerization crosslinkers serve as a sacrificial network primarily responsible for stress relaxation. The initial relaxation of **DN6** occurred during the second timeframe (∼7s) of the pause phase, with the hydrogel relaxing the mechanical load by ∼17% (Figure S16-17, Table S2). The second relaxation occurred around ∼249s with releasing a load of ∼88% The first relaxation time they stayed relatively constant for **DN1-3,** while the second relaxation stage reduced when the **SN** concentration increased. When polymer concentration increased to 2 wt%, the first relaxation time declined in **DN4-6** while the second relaxation was prolonged when the **SN** concentration increased. The shorter relaxation time could be attributed to the viscoelastic nature of the hydrogel resulting from the rapid fiber rupture. The longer relaxation time likely is connected to the network poroelasticity that originates from the loss of water in the gel. These results are likely related to the supramolecular polymer interactions and pore size of the network, demonstrating that the amount of polymer and supramolecular fiber network regulate its poroviscorelaxation behaviour. The augmentation of the **SN** concentration within the hydrogel corresponded to an increase in the relaxation amplitude, with relatively minimal alterations in the relaxation time.

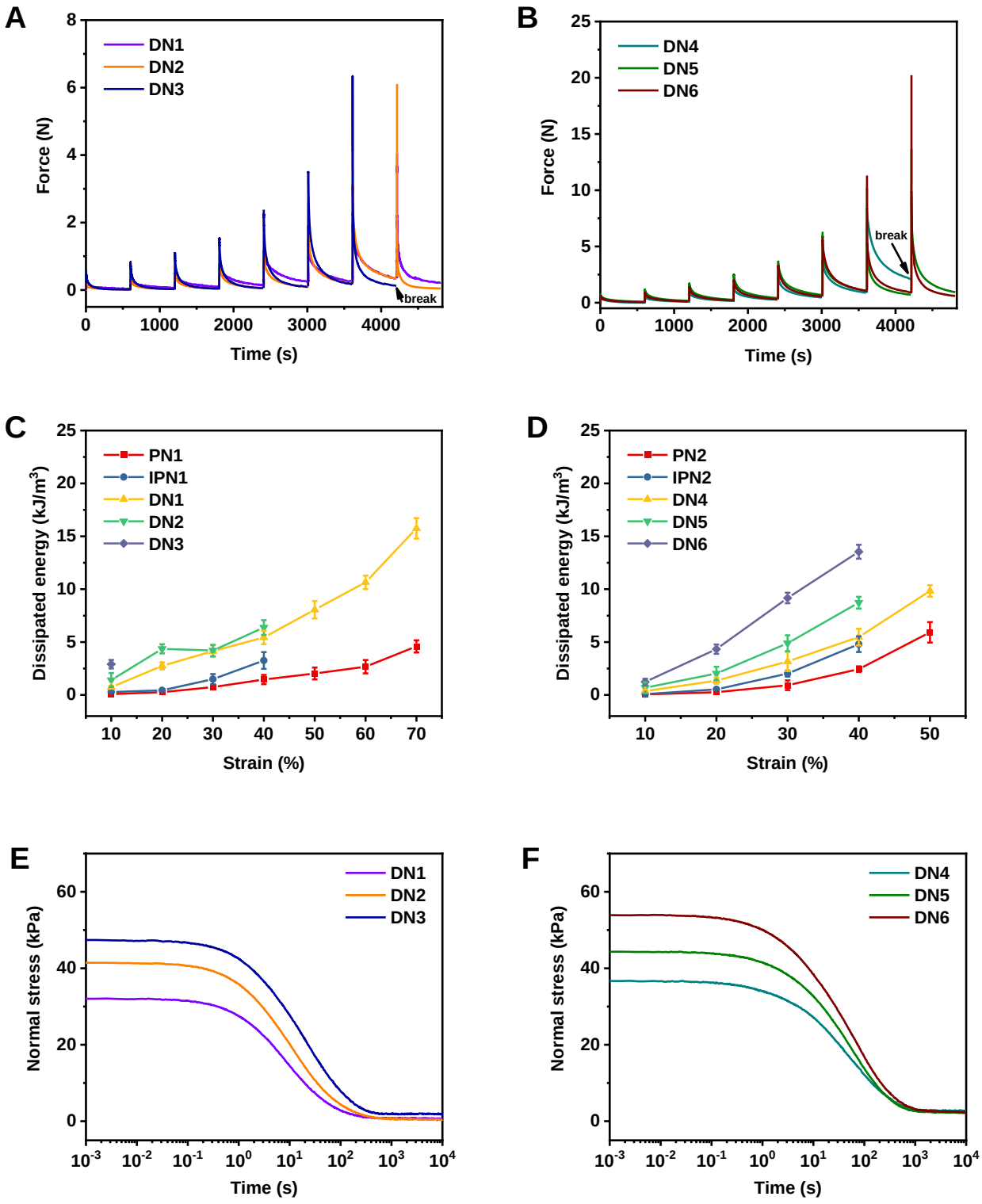

Figure 3. Step-stress relaxation curves of (A) **DN1-3**, and (B) **DN4-6** with increasing strain (5%) at the start of each loading cycle. Dissipated energy of at different maximum strains of (C) **PN1**, **IPN1** and **DN1-3**, (D) **PN2**, **IPN2** and **DN4-6** hydrogels, Mean ± SD, N ≥ 3. Poroviscorelaxation curves of (E) **DN1-3**, (F) **DN4-6** under 15% consistent normal strain.

Cross-sectional morphology and pore sizes of DN hybrid hydrogels

The pores of the hydrogel permit the exchange of oxygen and nutrients needed to sustain cell cultures.[63] Furthermore, their size and morphology will also affect the movement of water within the pores in response to an applied load impacting the mechanical behavior of the materials.[64] We imaged the pores by scanning electron microscopy (SEM) to check the pore structures and size from freeze-dried **DN** hydrogel cross-sections. The **DN** hydrogels exhibited pore structures with clear edges and a fibrous interconnected wall that supports the pores (Figure S18-19). The pore diameters fell within the range of ~13 µm - 21 µm and tended to decrease with a greater number of supramolecular filaments or polymer content, indicates that the incorporation of **SN** or **PN**, along with their crosslinking, in the **DN** hydrogels resulted in a reduction in pore size and a consequent increase gel mechanical properties as recorded in oscillatory rheology measurements. Transmission electron microscopy (TEM) images of diluted hydrogels **DN1** and **DN6** further confirmed their filament nanostructures (Figure S20).

The equilibrium water content (EWC) and stability under physiological conditions are critical features of hydrogel materials to determine for assessing their suitability for a given cell culture application.[65,66] We calculated the EWC for all crosslinked **DN1-6** and **PN1**-**2** hydrogels (Figure 4). All the hydrogels remained as gels after overnight equilibration before crosslinking, even with the addition of photoinitiators. After crosslinking by visible light (450 nm, LED) for 2 minutes, **PN1**-**2** hydrogels increased in weight by ~39 times - ~135 times leading to very high EWCs (~98% - ~100%). Owing to their higher network densities, **DN1** - **DN6** displayed slightly lower swelling ratios (29 - 45 times), and an EWC of ~96% - ~97%. Moreover, both **DN** and **PN** gels kept ~100% of their initial weight for 28 days showing little changes in mass or swelling ratio under physiological conditions. Gel inversion images on day 28 supports these measurements showing gels that are stable over the testing period. Overall, these **DN** hydrogels showed higher EWC than most other hydrogels, indicating their potential for long-term 3D cell culture.

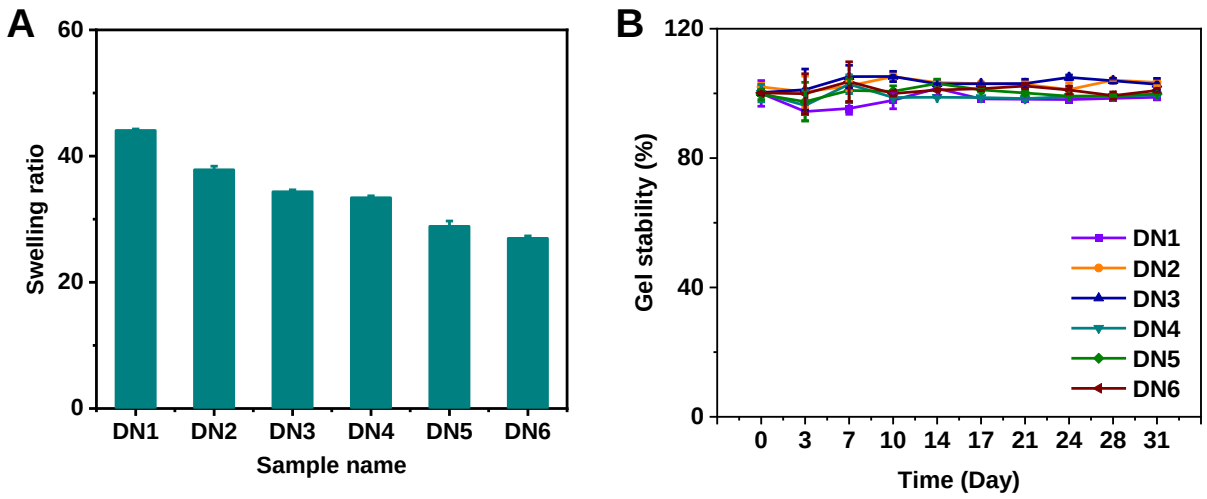

Figure 4. Characterization of **DN1-6** hydrogels. (A) Swelling ratios of photo-crosslinked **DN1-6** hydrogels in PBS after 24 hours. Mean ± SD, N ≥ 3. (B) Gel stability data of **DN1-6** hydrogels were kept in PBS at 37°C for 4 weeks. Mean ± SD, N ≥ 3.

Mechanical loading affects the matrix growth in 3D culture

To assess the suitability of visible-light-induced (450 nm) **DN** hybrid hydrogels as a synthetic platform for 3D cell culture applications, we first investigated cell viability of NIH 3T3 fibroblasts encapsulated within the hydrogels **DN1-6**. LIVE/DEAD staining revealed that all crosslinked **DN1-6** hydrogels exhibited high cell viability (>90% / 24h) (Figure S21-22). We then evaluated the viability of human primary articular chondrocytes (hPACs) within the materials. These primary cells also showed high cell viability (>90% / 24h, >80% / 48h) opening the door to examine the construction of 3D cartilage constructs within the materials *in vitro* (Figure S23-25).

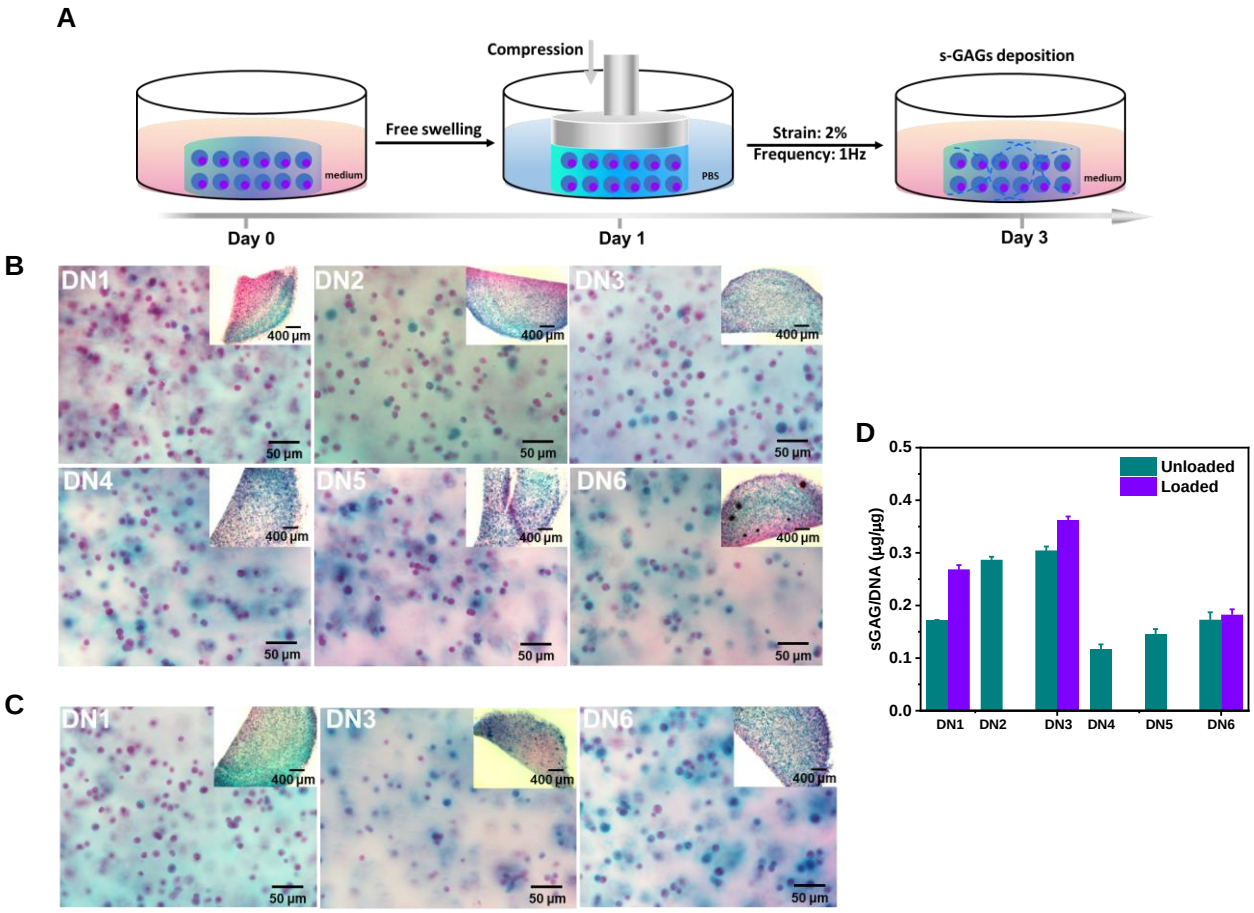

Figure 5. Influence of stiffness and soft loading on hPACs encapsulated in hydrogels **DN1-6**. (A) Scheme of hPACs-laden hydrogels and loading conditions during 3D chondrocyte culture. Alcian Blue staining for the s-GAGs with nuclear fast red counterstaining of hPACs in (B) crosslinked **DN1-6** hydrogels after 2 days culture in free swelling controls and (C) crosslinked **DN1, DN3** and **DN6** hydrogels after 2 days soft loading. Insert: an overview of hPACs-laden hydrogels. (D) s-GAGs deposition relative to DNA content using a DMMB assay. Visible light irradiation was applied through a benchtop of LED (~10 mW/cm^2, 450 nm).

Next, we investigated the effect of stiffness, a bioactive cue (SQ-RGD) and growth factor (TGF-β1) on hPACs by reading out matrix production within the gels.[1,67] Here we introduced a third monomer SQ-RGD based on C8-SQ with one arm modified with GGGRGDS peptide that binds cell surface integrins.[68] We stained the hPAC-laden hydrogels with Alcian Blue for sulfated-glycosaminoglycans (s-

GAGs) at the end of the culture period. **DN** hydrogels with the same polymer concentration, but with increased stiffness due to longer UV exposures showed increased degrees of matrix deposition. To further quantify matrix production, we performed the dimethyl-methylene blue (DMMB) assay. When comparing hydrogels **DN4**-**6**, **DN6** (~0.17 μg/μg) displayed the highest s-GAG quantity as compared to **DN5** (~0.14 μg/μg) and **DN4** (~0.12 μg/μg), which is on par with our previous results for hydrogel constructs of comparable stiffness (Figure 5). Hydrogels **DN1-3** exhibited a comparable pattern to **DN4-6**, but all of them demonstrated a higher level of s-GAGs deposition while maintaining an equivalent amount of the supramolecular network (**DN1**: ~0.17 μg/μg; **DN2**: ~0.28 μg/μg; **DN3**: ~0.30 μg/μg). In particular, **DN3** displayed the highest amount of s-GAG deposition among hydrogels **DN1-6**, surpassing **DN6** ~0.76 times and consistent with earlier reports suggesting that PEG hydrogels with excessive stiffness can hinder matrix deposition.[7,69,70] Removal of SQ-RGD in **DN6** did not impact matrix production in free swelling conditions, whereas the absence of TGF-β1 caused a noticeable decrease in s-GAGs deposition (Figure S26-27). Based on earlier reports that demonstrated the need for RGD peptides in mechanical loading experiments,[71] we used hydrogels **DN1-3** and **DN6** with 10% mole SQ-RGD for subsequent cyclic compressive loading experiments.

Cyclic compressive loading of the synthetic hydrogels *in vitro* can effectively enhance matrix production to mimic the native environment and stimulate biosynthesis in chondrocytes.[72-74] hPACs laden hydrogels (**DN1-3, DN6)** subjected to a soft compressive loading (2% strain, 1Hz) with a MACH-2 loading machine for two days (10 min/day) showed a pronounced effect on s-GAG deposition when compared to free swelling controls (**DN1**: ~0.27 μg/μg; **DN3**: ~0.36 μg/μg; **DN6**: ~0.18 μg/μg). Removal of SQ-RGD and TGF-β1 resulted in a slight increase in s-GAGs deposition consistent with the free swelling condition (Figure S26-27). Collectively, these results demonstrate that the **DN** hydrogels maintain the chondrogenic characteristics of hPACs and promote the generation of cartilaginous matrix with mechanical loading that can be useful for further exploration of these materials in chondrocyte culture.

4.3 Conclusion

We herein report the development of a supramolecular and covalent polymer-based **DN** hydrogel that can be applied for 3D chondrocyte culture with cyclic compressive loading. Rapid visible light photopolymerization between supramolecular and covalent networks using phenol chemistry yielded a double network hydrogel with covalent and non-covalent crosslinking strategies. Remarkably, the incorporation of filamentous supramolecular structures in the materials enhanced stress relaxation in both the shear and axial directions, even with increasing stiffness. The ratio of these chemical bonds could be tuned by the filamentous supramolecular and poly(ethylene glycol) network concentrations, therefore influencing the complex mechanics of the materials including their stress relaxation properties. The high compressive and fast, biomimetic stress relaxation behaviour of **DN** hydrogels permitted them to withstand cyclic compressive loads for 3D human primary articular chondrocytes culture. After two days of cyclic loading, the chondrocytes deposited crucial cartilage ECM polysaccharides and proteins as compared to the free swelling condition. Importantly, this visible-light induced phenol photopolymerization holds promise for fabricating mechanically enhanced double network hydrogels, particularly advantageous for supporting those sensitive 3D cell cultivation within dynamically loaded environments.

Reference

(1) Mostakhdemin, M.; Nand, A.; Ramezani, M. Articular and Artificial Cartilage, Characteristics, Properties and Testing Approaches-A Review. *Polymers (Basel)* **2021,** *13*, 2000.

(2) Makris, E. A.; Gomoll, A. H.; Malizos, K. N.; Hu, J. C.; Athanasiou, K. A. Repair and tissue engineering techniques for articular cartilage. *Nat Rev Rheumatol* **2015,** *11* (1), 21.

(3) Freedman, B. R.; Mooney, D. J. Biomaterials to Mimic and Heal Connective Tissues. *Adv. Mater.* **2019,** *31* (19), e1806695.

(4) Zhou, L.; Guo, P.; D'Este, M.; Tong, W.; Xu, J.; Yao, H.; Stoddart, M. J.; van Osch, G. J. V. M.; Ho, K. K.-W.; Li, Z.et al. Functionalized Hydrogels for Articular Cartilage Tissue Engineering. *Engineering* **2022,** *13*, 71.

(5) Yang, X.; Li, S.; Ren, Y.; Qiang, L.; Liu, Y.; Wang, J.; Dai, K. 3D printed hydrogel for articular cartilage regeneration. *Composites Part B: Engineering* **2022,** *237*, 109863.

(6) Wilusz, R. E.; Sanchez-Adams, J.; Guilak, F. The structure and function of the pericellular matrix of articular cartilage. *Matrix Biol.* **2014,** *39*, 25.

(7) Loebel, C.; Kwon, M. Y.; Wang, C.; Han, L.; Mauck, R. L.; Burdick, J. A. Metabolic labeling to probe the spatiotemporal accumulation of matrix at the chondrocyte–hydrogel interface. *Adv. Funct. Mater.* **2020,** *30* (44), 1909802.

(8) Guilak, F.; Nims, R. J.; Dicks, A.; Wu, C.-L.; Meulenbelt, I. Osteoarthritis as a disease of the cartilage pericellular matrix. *Matrix Biol.* **2018,** *71*, 40.

(9) Alexopoulos, L. G.; Williams, G. M.; Upton, M. L.; Setton, L. A.; Guilak, F. Osteoarthritic changes in the biphasic mechanical properties of the chondrocyte pericellular matrix in articular cartilage. *Journal of biomechanics* **2005,** *38* (3), 509.

(10) Yu, P.; Li, Y.; Sun, H.; Ke, X.; Xing, J.; Zhao, Y.; Xu, X.; Qin, M.; Xie, J.; Li, J. Cartilage-Inspired Hydrogel with Mechanical Adaptability, Controllable Lubrication, and Inflammation Regulation Abilities. *ACS Appl. Mater. Interfaces* **2022**, *14*, 27360.

(11) Timmermans, R. G. M.; Bloks, N. G. C.; Tuerlings, M.; van Hoolwerff, M.; Nelissen, R. G. H. H.; van der Wal, R. J. P.; van der Kraan, P. M.; Blom, A. B.; van den Bosch, M. H. J.; Ramos, Y. F. M.et al. A human *in vitro* 3D neo-cartilage model to explore the response of OA risk genes to hyper-physiological mechanical stress. *Osteoarthritis and Cartilage Open* **2022,** *4* (1), 100231.

(12) Caccavo, D.; Lamberti, G. PoroViscoElastic model to describe hydrogels' behavior. *Mater Sci Eng C Mater Biol Appl* **2017,** *76*, 102.

(13) Wang, Q.-M.; Mohan, A. C.; Oyen, M. L.; Zhao, X.-H. Separating viscoelasticity and poroelasticity of gels with different length and time scales. *Acta Mechanica Sinica* **2014,** *30* (1), 20.

(14) Nia, H. T.; Han, L.; Li, Y.; Ortiz, C.; Grodzinsky, A. Poroelasticity of cartilage at the nanoscale. *Biophys. J.* **2011,** *101* (9), 2304.

(15) Han, L.; Wang, M.; Li, P.; Gan, D.; Yan, L.; Xu, J.; Wang, K.; Fang, L.; Chan, C. W.; Zhang, H.et al. Mussel-Inspired Tissue-Adhesive Hydrogel Based on the Polydopamine-Chondroitin Sulfate Complex for Growth-Factor-Free Cartilage Regeneration. *ACS Appl. Mater. Interfaces* **2018,** *10* (33), 28015.

(16) Huang, D.; Huang, Y.; Xiao, Y.; Yang, X.; Lin, H.; Feng, G.; Zhu, X.; Zhang, X. Viscoelasticity in natural tissues and engineered scaffolds for tissue reconstruction. *Acta Biomater* **2019,** *97*, 74.

(17) Li, W.; Wu, D.; Hu, D.; Zhu, S.; Pan, C.; Jiao, Y.; Li, L.; Luo, B.; Zhou, C.; Lu, L. Stress-relaxing double-network hydrogel for chondrogenic differentiation of stem cells. *Mater Sci Eng C Mater Biol Appl* **2020,** *107*, 110333.

(18) Chaudhuri, O.; Cooper-White, J.; Janmey, P. A.; Mooney, D. J.; Shenoy, V. B. Effects of extracellular matrix viscoelasticity on cellular behaviour. *Nature* **2020,** *584* (7822), 535.

(19) Han, G.; Chowdhury, U.; Eriten, M.; Henak, C. R. Relaxation capacity of cartilage is a critical factor in rate- and integrity-dependent fracture. *Sci Rep* **2021,** *11* (1), 9527.
(20) Ma, C.; Du, T.; Niu, X.; Fan, Y. Biomechanics and mechanobiology of the bone matrix. *Bone Res.* **2022,** *10* (1), 59.
(21) Zhao, X.; Chen, X.; Yuk, H.; Lin, S.; Liu, X.; Parada, G. Soft Materials by Design: Unconventional Polymer Networks Give Extreme Properties. *Chem Rev* **2021,** *121* (8), 4309.
(22) Gu, Z.; Huang, K.; Luo, Y.; Zhang, L.; Kuang, T.; Chen, Z.; Liao, G. Double network hydrogel for tissue engineering. *Wiley Interdiscip Rev Nanomed Nanobiotechnol* **2018,** *10* (6), e1520.
(23) Sun, W.; Xue, B.; Li, Y.; Qin, M.; Wu, J.; Lu, K.; Wu, J.; Cao, Y.; Jiang, Q.; Wang, W. Polymer-Supramolecular Polymer Double-Network Hydrogel. *Adv. Funct. Mater.* **2016,** *26* (48), 9044.
(24) Rodell, C. B.; Dusaj, N. N.; Highley, C. B.; Burdick, J. A. Injectable and Cytocompatible Tough Double-Network Hydrogels through Tandem Supramolecular and Covalent Crosslinking. *Adv. Mater.* **2016,** *28* (38), 8419.
(25) Wang, H.; Zhu, D.; Paul, A.; Cai, L.; Enejder, A.; Yang, F.; Heilshorn, S. C. Covalently adaptable elastin-like protein - hyaluronic acid (ELP - HA) hybrid hydrogels with secondary thermoresponsive crosslinking for injectable stem cell delivery. *Adv. Funct. Mater.* **2017,** *27* , 1605609.
(26) Li, L.; Zhang, K.; Wang, T.; Wang, P.; Xue, B.; Cao, Y.; Zhu, L.; Jiang, Q. Biofabrication of a biomimetic supramolecular-polymer double network hydrogel for cartilage regeneration. *Materials & Design* **2020,** *189,* 108492.
(27) Hilderbrand, A. M.; Ford, E. M.; Guo, C.; Sloppy, J. D.; Kloxin, A. M. Hierarchically structured hydrogels utilizing multifunctional assembling peptides for 3D cell culture. *Biomater Sci* **2020,** *8* (5), 1256.
(28) Huang, L.; Abdalla, A. M. E.; Xiao, L.; Yang, G. Biopolymer-Based Microcarriers for Three-Dimensional Cell Culture and Engineered Tissue Formation. *Int J Mol Sci* **2020,** *21*, 1895.
(29) Feng, Z.; Zhao, J.; Li, Y.; Xu, S.; Zhou, J.; Zhang, J.; Deng, L.; Dong, A. Temperature-responsive in situ nanoparticle hydrogels based on hydrophilic pendant cyclic ether modified PEG-PCL-PEG. *Biomater Sci* **2016,** *4* (10), 1493.
(30) Tamesue, S.; Noguchi, S.; Kimura, Y.; Endo, T. Reversing Redox Responsiveness of Hydrogels due to Supramolecular Interactions by Utilizing Double-Network Structures. *ACS Appl Mater Interfaces* **2018,** *10* (32), 27381.
(31) Loebel, C.; Ayoub, A.; Galarraga, J. H.; Kossover, O.; Simaan-Yameen, H.; Seliktar, D.; Burdick, J. A. Tailoring supramolecular guest-host hydrogel viscoelasticity with covalent fibrinogen double networks. *J Mater Chem B* **2019,** *7* (10), 1753.
(32) Ouyang, L.; Highley, C. B.; Rodell, C. B.; Sun, W.; Burdick, J. A. 3D Printing of Shear-Thinning Hyaluronic Acid Hydrogels with Secondary Cross-Linking. *ACS Biomaterials Science & Engineering* **2016,** *2* (10), 1743.
(33) Richardson, B. M.; Walker, C. J.; Maples, M. M.; Randolph, M. A.; Bryant, S. J.; Anseth, K. S. Mechanobiological Interactions between Dynamic Compressive Loading and Viscoelasticity on Chondrocytes in Hydrazone Covalent Adaptable Networks for Cartilage Tissue Engineering. *Adv Healthc Mater* **2021,** *10* (9), e2002030.
(34) Richardson, B. M.; Walker, C. J.; Macdougall, L. J.; Hoye, J. W.; Randolph, M. A.; Bryant, S. J.; Anseth, K. S. Viscoelasticity of hydrazone crosslinked poly(ethylene glycol) hydrogels directs chondrocyte morphology during mechanical deformation. *Biomater Sci* **2020,** *8* (14), 3804.
(35) Chen, F. H.; Rousche, K. T.; Tuan, R. S. Technology Insight: adult stem cells in cartilage regeneration and tissue engineering. *Nat Clin Pract Rheumatol* **2006,** *2* (7), 373.
(36) Sophia Fox, A. J.; Bedi, A.; Rodeo, S. A. The basic science of articular cartilage: structure, composition, and function. *Sports Health* **2009,** *1* (6), 461.

(37) Soltanahmadi, S.; Raske, N.; de Boer, G. N.; Neville, A.; Hewson, R. W.; Bryant, M. G. Fabrication of Cartilage-Inspired Hydrogel/Entangled Polymer–Elastomer Structures Possessing Poro-Elastic Properties. *ACS Applied Polymer Materials* **2021,** *3* (5), 2694.
(38) Shirazi, R.; Shirazi-Adl, A.; Hurtig, M. Role of cartilage collagen fibrils networks in knee joint biomechanics under compression. *J Biomech* **2008,** *41* (16), 3340.
(39) Han, L.; Grodzinsky, A. J.; Ortiz, C. Nanomechanics of the Cartilage Extracellular Matrix. *Annu Rev Mater Res* **2011,** *41*, 133.
(40) Lim, K. S.; Galarraga, J. H.; Cui, X.; Lindberg, G. C.; Burdick, J. A.; Woodfield, T. B. Fundamentals and applications of photo-cross-linking in bioprinting. *Chem. Rev.* **2020,** *120* (19), 10662.
(41) Zhu, Y.; Chen, J.; Liu, H.; Zhang, W. Photo-cross-linked Hydrogels for Cartilage and Osteochondral Repair. *ACS Biomaterials Science & Engineering* **2023,** *9* (12), 6567.
(42) Summonte, S.; Racaniello, G. F.; Lopedota, A.; Denora, N.; Bernkop-Schnürch, A. Thiolated polymeric hydrogels for biomedical application: Cross-linking mechanisms. *J. Controlled Release* **2021,** *330*, 470.
(43) Muir, V. G.; Burdick, J. A. Chemically modified biopolymers for the formation of biomedical hydrogels. *Chem. Rev.* **2020,** *121* (18), 10908.
(44) Zheng, Z.; Eglin, D.; Alini, M.; Richards, G. R.; Qin, L.; Lai, Y. Visible light-induced 3D bioprinting technologies and corresponding bioink materials for tissue engineering: a review. *Engineering* **2021,** *7* (7), 966.
(45) Li, X.; Li, Y.; Zhang, X.; Xu, J.; Kang, J.; Li, B.; Zhao, B.; Wang, L. Cross-Linking Methods of the Silk Protein Hydrogel in Oral and Craniomaxillofacial Tissue Regeneration. *Tissue Engineering and Regenerative Medicine* **2024**, *1*, 529.
(46) Tong, C.; Liu, T.; Saez Talens, V.; Noteborn, W. E.; Sharp, T. H.; Hendrix, M. M.; Voets, I. K.; Mummery, C. L.; Orlova, V. V.; Kieltyka, R. E. Squaramide-based supramolecular materials for three-dimensional cell culture of human induced pluripotent stem cells and their derivatives. *Biomacromolecules* **2018,** *19* (4), 1091.
(47) Tong, C.; Liu, T.; Saez Talens, V.; Noteborn, W. E. M.; Sharp, T. H.; Hendrix, M.; Voets, I. K.; Mummery, C. L.; Orlova, V. V.; Kieltyka, R. E. Squaramide-Based Supramolecular Materials for Three-Dimensional Cell Culture of Human Induced Pluripotent Stem Cells and Their Derivatives. *Biomacromolecules* **2018,** *19* (4), 1091.
(48) Tong, C.; Wondergem, J. A. J.; Heinrich, D.; Kieltyka, R. E. Photopatternable, Branched Polymer Hydrogels Based on Linear Macromonomers for 3D Cell Culture Applications. *ACS Macro Lett.* **2020,** *9* (6), 882.
(49) Fairbanks, B. D.; Schwartz, M. P.; Halevi, A. E.; Nuttelman, C. R.; Bowman, C. N.; Anseth, K. S. A versatile synthetic extracellular matrix mimic via thiol-norbornene photopolymerization. *Advanced materials* **2009,** *21* (48), 5005.
(50) Means, A. K.; Grunlan, M. A. Modern Strategies To Achieve Tissue-Mimetic, Mechanically Robust Hydrogels. *ACS Macro Lett* **2019,** *8* (6), 705.
(51) Tang, S.; Richardson, B. M.; Anseth, K. S. Dynamic covalent hydrogels as biomaterials to mimic the viscoelasticity of soft tissues. *Prog. Mater Sci.* **2021,** *120*, 100738.
(52) Chaudhuri, O. Viscoelastic hydrogels for 3D cell culture. *Biomaterials science* **2017,** *5* (8), 1480.
(53) Sanchez-Adams, J.; Leddy, H. A.; McNulty, A. L.; O'Conor, C. J.; Guilak, F. The mechanobiology of articular cartilage: bearing the burden of osteoarthritis. *Curr. Rheumatol. Rep.* **2014,** *16* (10), 451.
(54) Doi, M. Gel dynamics. *J. Phys. Soc. Jpn.* **2009,** *78* (5), 052001.
(55) Yamaue, T. The stress diffusion coupling in the swelling dynamics of cylindrical gels. *The Journal of chemical physics* **2005,** *122* (8), 3466.
(56) Mow, V. C.; Wang, C. C.; Hung, C. T. The extracellular matrix, interstitial fluid and ions as a mechanical signal transducer in articular cartilage. *Osteoarthritis and Cartilage* **1999,** *7* (1), 41.

(57) Jahn, S.; Seror, J.; Klein, J. Lubrication of articular cartilage. *Annual review of biomedical engineering* **2016,** *18*, 235.
(58) June, R. K.; Mejia, K. L.; Barone, J. R.; Fyhrie, D. P. Cartilage stress-relaxation is affected by both the charge concentration and valence of solution cations. *Osteoarthritis Cartilage* **2009,** *17* (5), 669.
(59) Khayyeri, H.; Gustafsson, A.; Heuijerjans, A.; Matikainen, M. K.; Julkunen, P.; Eliasson, P.; Aspenberg, P.; Isaksson, H. A fibre-reinforced poroviscoelastic model accurately describes the biomechanical behaviour of the rat Achilles tendon. *PLoS One* **2015,** *10* (6), e0126869.
(60) Oftadeh, R.; Connizzo, B. K.; Nia, H. T.; Ortiz, C.; Grodzinsky, A. J. Biological connective tissues exhibit viscoelastic and poroelastic behavior at different frequency regimes: Application to tendon and skin biophysics. *Acta Biomater* **2018,** *70*, 249.
(61) Oyen, M. L. Mechanical characterisation of hydrogel materials. *Int. Mater. Rev.* **2013,** *59* (1), 44.
(62) Han, G.; Hess, C.; Eriten, M.; Henak, C. R. Uncoupled poroelastic and intrinsic viscoelastic dissipation in cartilage. *J Mech Behav Biomed Mater* **2018,** *84*, 28.
(63) Leal-Egaña, A.; Braumann, U.-D.; Díaz-Cuenca, A.; Nowicki, M.; Bader, A. Determination of pore size distribution at the cell-hydrogel interface. *Journal of nanobiotechnology* **2011,** *9* (1), 1.
(64) Loh, Q. L.; Choong, C. Three-dimensional scaffolds for tissue engineering applications: role of porosity and pore size. *Tissue Eng Part B Rev* **2013,** *19* (6), 485.
(65) Kerin, A.; Wisnom, M.; Adams, M. The compressive strength of articular cartilage. *Proc. Inst. Mech. Eng. H: J. Eng. Med.* **1998,** *212* (4), 273.
(66) Maganaris, C. N.; Paul, J. P.; J. Physiol., 1999.
(67) Huang, G.; Li, F.; Zhao, X.; Ma, Y.; Li, Y.; Lin, M.; Jin, G.; Lu, T. J.; Genin, G. M.; Xu, F. Functional and Biomimetic Materials for Engineering of the Three-Dimensional Cell Microenvironment. *Chem. Rev.* **2017,** *117* (20), 12764.
(68) Tong, C.; Wondergem, J. A. J.; van den Brink, M.; Kwakernaak, M. C.; Chen, Y.; Hendrix, M.; Voets, I. K.; Danen, E. H. J.; Le Devedec, S.; Heinrich, D.et al. Spatial and Temporal Modulation of Cell Instructive Cues in a Filamentous Supramolecular Biomaterial. *ACS Appl. Mater. Interfaces* **2022,** *14* (15), 17042.
(69) Lee, H.-p.; Gu, L.; Mooney, D. J.; Levenston, M. E.; Chaudhuri, O. Mechanical confinement regulates cartilage matrix formation by chondrocytes. *Nat. Mater.* **2017,** *16* (12), 1243.
(70) Tan, Y.; Huang, H.; Ayers, D. C.; Song, J. Modulating viscoelasticity, stiffness, and degradation of synthetic cellular niches via stoichiometric tuning of covalent versus dynamic noncovalent cross-linking. *ACS central science* **2018,** *4* (8), 971.
(71) Villanueva, I.; Weigel, C. A.; Bryant, S. J. Cell–matrix interactions and dynamic mechanical loading influence chondrocyte gene expression and bioactivity in PEG-RGD hydrogels. *Acta Biomater.* **2009,** *5* (8), 2832.
(72) Chen, C.; Tambe, D. T.; Deng, L.; Yang, L. Biomechanical properties and mechanobiology of the articular chondrocyte. *American Journal of Physiology-Cell Physiology* **2013,** *305* (12), C1202.
(73) Mauck, R. L.; Soltz, M. A.; Wang, C. C.; Wong, D. D.; Chao, P.-H. G.; Valhmu, W. B.; Hung, C. T.; Ateshian, G. A. Functional tissue engineering of articular cartilage through dynamic loading of chondrocyte-seeded agarose gels. *J. Biomech. Eng.* **2000,** *122* (3), 252.
(74) Bryant, S. J.; Chowdhury, T. T.; Lee, D. A.; Bader, D. L.; Anseth, K. S. Crosslinking density influences chondrocyte metabolism in dynamically loaded photocrosslinked poly (ethylene glycol) hydrogels. *Annals of biomedical engineering* **2004,** *32*, 407.

Supporting information

S4.1 Materials and methods

Materials

4 arm-poly(ethylene glycol) (4arm-PEG-OH, Mw: 10 kDa) was purchased from JenKem Technology. Deuterated solvents for NMR experiments were obtained from Euriso-top. Water was deionized before use. Formvar/Carbon 200 Mesh Copper grids were purchased from Electron Microscopy Sciences. Dulbecco's modified Eagle medium (DMEM) was received from Gibco, Life Technologies. Fetal bovine serum (FBS) was achieved from Biowest. The antibiotics penicillin and streptomycin were purchased from Gibco. µ-Slide 15 Well 3D chambered cover plates were purchased from Ibidi. N, N'-Dicyclohexylcarbodiimide, piperidine, Dulbecco's phosphate-buffered saline (DPBS, pH=7.4), calcein AM, propidium iodide (PI), Alcian Blue 8-GX, nuclear fast red-aluminum sulfate and all other commercially available chemicals were obtained from Sigma Aldrich at the highest purity available and directly used without further purification. 3-(4-(tert-butoxy)phenyl)propanoic acid,[1] monomers **C8-SQ**, **SQ-RGD**, **PEG-TOS (4)**, **PEG-N_3 (5)**, **C8-CBZ (6)** were synthesized as previously described[2]. Milli-Q water was employed for all the experiments. All compounds were stored at -20°C before use.

Methods

^{1}H-NMR and ^{13}C-NMR spectra were collected at room temperature (RT) on a Bruker DMX-400. All supramolecular monomers were purified by high-performance liquid chromatography (HPLC) on a Shimadzu system equipped with two LC-20AR pumps, an SPD-20A UV-Vis detector and a Phenomenex Kinetex EVO C18 column. The mobile phases were CH_3CN and H_2O with 0.1% trifluoroacetic acid. Liquid chromatography-mass spectrometry (LC-MS) analysis was performed on a Finnigan Surveyor HPLC system (with UV-Vis detection from 200-600 nm) equipped with a Gemini C18 50 x 4.60 mm reverse phase column coupled to Finnigan LCQ Advantage Max mass spectrometer with ESI. A gradient of 10-90% of CH_3CN/H_2O with 0.1% trifluoroacetic acid over 13.5 minutes was used for the mobile phase. The supramolecular fibers were imaged on a JEOL JEM-1400 Plus transmission electron microscope (TEM). The surface morphology and pore sizes of the lyophilized hydrogels were imaged by scanning electron microscope (SEM). Oscillatory rheology experiments were performed on a Discovery Hybrid Rheometer (DHR-2) from TA Instruments with a Smart Swap visible light assembly with a quartz lower plate (20 mm) and an aluminum upper plate (8 mm) at RT at a fixed gap of 500 µm, visible light was applied through an OmniCure S2000 high-pressure mercury light source with a filter (λ = 400-500 nm, primary peak: 450 nm) equipped from Excelitas connected to the rheometer through a light guide (5 mm diameter). The visible light intensity was calibrated using an OmniCure radiometer sensor accessory. Compression experiments were performed under the same conditions on the rheometer but with a fixed gap of 1.2 mm and a maximum axial force of 50 N. Both NIH 3T3 fibroblast cells and human primary articular chondrocytes (hPACs)were cultured in Dubecco's modified Eagle medium (DMEM) with high glucose, with 10% fetal calf serum, 0.1% GlutaMAX, 0.2% penicillin and 0.2% streptomycin. hPACs were counted on NucleoCounter NC-200 from ChemoMetec. Images to assess cell viability in 3D cultures were captured on an LSM 710 confocal laser scanning microscope from Zeiss. Compressive mechanical loading of the 3D cell cultures in the hydrogels were performed continuously in cycles at RT on a MACH-

1 mechanical tester from Biomomentum. Confocal fluorescent images of immunostained 3D cell cultures were acquired on a Stellaris 8 confocal laser scanning microscope from Leica with a white light laser (440-790 nm) and Power HyD detectors. Alcian Blue staining images were taken in brightfield on a light microscope from Olympus. A microplate reader from BioTek Synergy HT was used to quantify sulfated glycosaminoglycan (s-GAGs) content through the dimethyl methylene blue (DMMB) assay using measured absorbance values at 525 and 595 nm. A benchtop LED light (~10 mW/cm², 450 nm) was employed to initiate crosslinking in all other samples except for the ones on the rheometer.

Synthetic routes

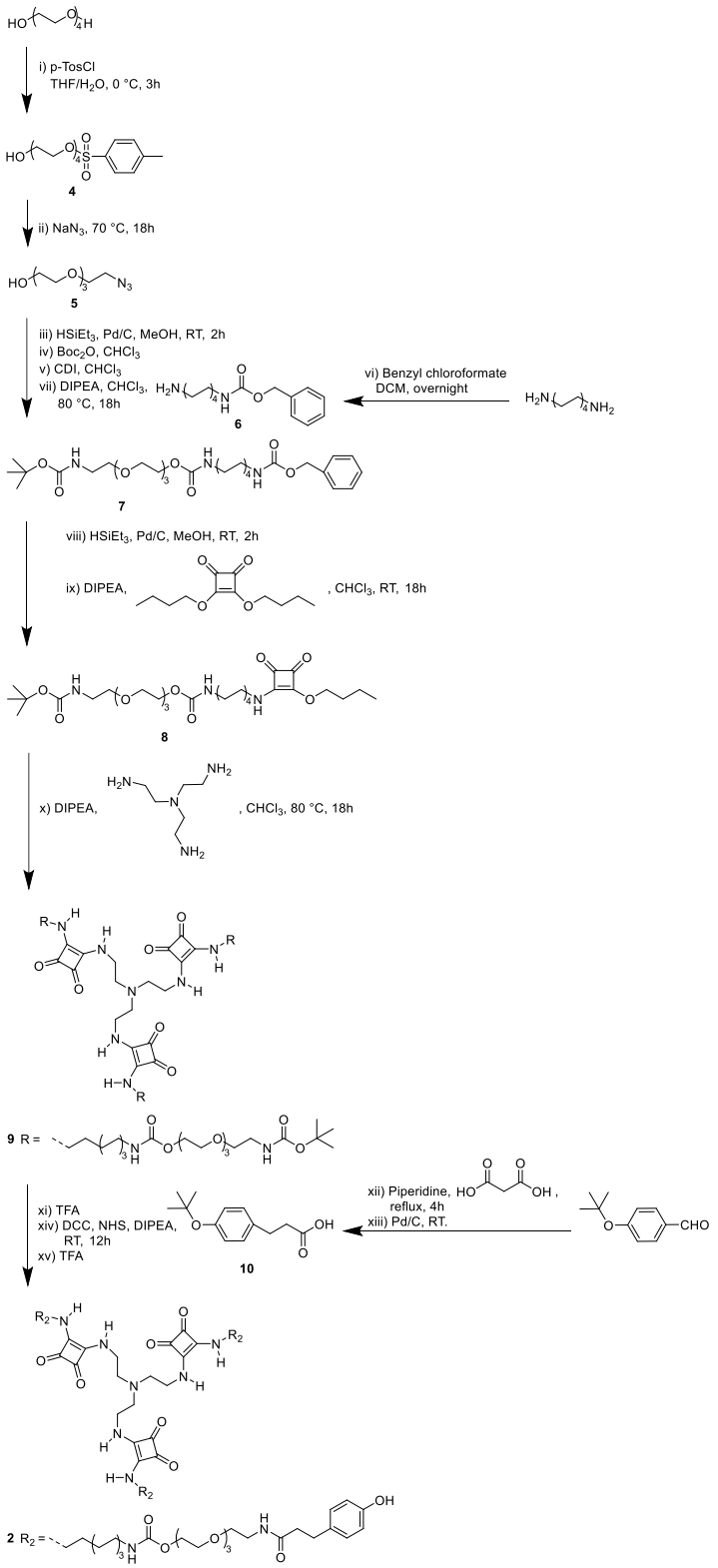

Figure S1. Synthetic route of monomer **SQ-Phe (2)**.

Synthetic procedures

Synthesis of 7

5 (2.68 g, 12.37 mmol) was dissolved in dry CH_3OH (5 mL), palladium on carbon (100.0 mg, 0.9 mmol) was added and degassed with N_2 for 10 min. Triethylsilane (3.95 mL, 24.74 mmol) was added dropwise and left stirring at RT for 2 hours, filtered through Celite, washed with CH_3OH, and concentrated to yield a clear oil which was used directly. $CHCl_3$ (20 mL) was added to the crude, followed by adding boc-anhydride (2.98 g, 13.64 mmol) and DIPEA (3.23 mL, 18.56 mmol) under RT for 3 hours before using rotary evaporation to concentrate which was used directly. The intermediate was confirmed by TLC. 1,1'-carbonyldiimidazole (3.02 g, 18.56 mmol) was added to the reaction of intermediate at RT stirring for 1h. The activated intermediate was verified by TLC. **6** (4.80 g, 17.2 mmol, 1.5 equiv) and $CHCl_3$ (20 mL) was added to the activated intermediate and the mixture was heated to reflux at 80°C overnight. Once the reaction was finished, $CHCl_3$ (30 mL) was added and washed 3x with water. The organic layers were combined, dried with sodium sulfate, and concentrated. The concentrate was purified using silica column chromatography (CH_2Cl_2/EtOAc, 99/1-95/5-90/10, v/v) and dried under vacuum to afford the product as a white solid.

Yield: 33.13%, 2.45 g. ^{1}H-NMR ($CDCl_3$, 400 MHz): 7.36-7.29 (m, 5H), 5.09 (s, 2H), 4.97 (br s, 1H), 4.91 (br s, 1H), 4.22-4.19 (m, 2H), 3.74-3.52 (m, 12H), 3.32-3.29 (m, 2H), 3.20-3.12 (m, 4H), 1.5-1.47 (m, 12H), 1.32-1.29 (m, 9H). ^{13}C-NMR ($CDCl_3$, 100 MHz): 156.59, 137.19, 130.21, 128.68, 128.25, 117.33, 85.91, 70.74, 70.67, 70.44, 69.88, 66.72, 63.95, 41.22, 40.54, 30.08, 29.29, 28.60, 28.06, 26.79. HRMS (ESI) m/z: $[M+H]^+$ calcd. for $C_{30}H_{52}N_3O_9$ 598.36981; found: 598.36931. LC-MS: t=7.73 min, m/z: 620.23 $[M+Na]^+$.

Synthesis of 8

Palladium on carbon (80.0 mg, 0.72 mmol) was added to a solution of **7** (0.933 g, 1.56 mmol) in dry CH_3OH (5 mL) and degassed with N_2 for 10 min. Triethylsilane (2.45 mL, 3.12 mmol) was added dropwise and left stirring at RT for 2 hours, filtered through Celite, washed with CH_3OH, concentrated and used directly. 3,4-dibutoxy-3-cyclobutene-1,2-dione (0.40 mL, 1.87 mmol) and DIPEA (992.87 µL, 5.7 mmol) were added into the intermediate dissolved in $CHCl_3$ (20 mL) and heated to reflux at 80°C overnight, $CHCl_3$ (30 mL) was added and extracted 3x with $CHCl_3$. The organic layers were combined, dried with sodium sulfate, and concentrated. The concentrate was purified using silica column chromatography (Pet ether/EtOAc, 10/90-90/10, v/v) and dried under vacuum to afford the product as a white solid.

Yield: 56.32%, 541.81 mg. ^{1}H-NMR ($CDCl_3$, 400 MHz): 7.82-7.78 (t, 1H), 5.50-5.47 (br s, 1H), 5.42-5.39 (br s, 1H), 4.76-4.72 (t, 2H), 4.24-4.18 (m, 2H), 3.73-3.55 (m, 12H), 3.45-3.40 (m, 2H), 3.32-3.28(m, 2H), 3.16-3.11 (m, 2H), 1.83-1.73 (m, 2H), 1.66-1.59 (m, 2H), 1.51-1.24 (m, 21H), 1.00-0.93 (m, 3H). ^{13}C-NMR ($CDCl_3$, 100 MHz): 189.18, 188.63, 182.76, 182.46, 176.77, 172.57, 172.33, 156.25, 155.80, 78.61, 72.84, 70.12, 70.08, 69.77, 69.22, 63.81, 63.36, 60.01, 44.43, 44.21, 40.57, 39.98, 31.65, 30.61, 30.21, 29.51, 28.75, 28.68, 28.06, 26.27, 25.96, 18.29, 18.17, 13.33. HRMS (ESI) m/z: $[M+H]^+$ calcd. for $C_{30}H_{54}N_3O_{10}$: 616.38037; found: 616.38008. LC-MS: t=7.33 min, m/z: found: 616.48 $[M+H]^+$.

Synthesis of 9

Tris(2-aminoethyl)amine (46.06 mg, 0.32 mmol) and DIPEA (167.22 µL, 0.96 mmol) were added into a solution of **8** (642.10 g, 1.04 mmol) dissolved in $CHCl_3$ (20 mL) under nitrogen. The reaction mixture was on reflux at 80°C overnight, concentrated and purified on silica column chromatography (EtOAc/CH_3OH-CH_2Cl_2/CH_3OH, 100/00-80/20, v/v). The product was concentrated by rotary evaporation and dried in a vacuum overnight to obtain a brownish oil.

Yield: 42.9%, 23.92 mg. ^{1}H-NMR (DMSO-d_6, 400 MHz): 7.73 (br s, 5H), 5.37-5.11 (m, 5H), 4.20-4.17 (m, 6H), 3.77-3.51 (m, 48H), 3.31-3.27 (m, 6H), 3.13-3.08(m, 6H), 2.71 (br s, 4H), 2.28 (br s, 2H), 1.61-1.26 (m, 63H). ^{13}C-NMR (DMSO-d_6, 100 MHz): 182.94, 169.22, 167.11, 156.66, 156.29, 79.34, 70.69, 70.61, 70.46, 70.35, 69.84, 63.90, 54.52, 44.83, 42.74, 41.17, 40.52, 31.26, 30.09, 29.40, 28.59, 26.90, 26.63, 18.98, 17.67, 12.62. HRMS (ESI) m/z: $[M+H]^+$ calcd. for $C_{84}H_{148}N_{13}O_{27}$: 1771.06021; found: 1771.06021. LC-MS: t= 6.77 min, m/z: 1770.20 $[M]^+$.

Synthesis of 10

10 was synthesized according to a published protocol[1]. In detail, 4-(tert-butoxy)benzaldehyde (1.22 mL, 7.05 mmol) was dissolved in pyridine (20 mL) under a nitrogen flow, and malonic acid (1.10 g, 10.53 mmol) was added. 10 min later, piperidine (207.51 µL, 2.10 mmol) was added dropwise and the solution was refluxed for 3 h. Afterward, hydrochloric acid (8 mL, 1 M) was used to acidify the solution extracted 3x with EtOAc (25 mL). The organics were combined, dried with sodium sulfate, and concentrated to obtain a yellowish solid. Next, the obtained yellowish solid was dissolved in dry THF (25 mL), palladium on carbon (500 mg, 4.69 mmol) was added and the mixture was stirred under a hydrogen balloon overnight, filtered through Celite, extracted with CH_2Cl_2 and CH_3OH, and concentrated. The concentrate was purified on silica column chromatography (EtOAc/n-hexanes, 90/10-50/50, v/v). The product was concentrated by rotary evaporation and dried in a vacuum overnight to obtain a white solid.

Yield: 42.9%, 2.5 g. ^{1}H-NMR (DMSO-d_6, 400 MHz): 7.15-7.09 (d, 2H), 6.90-6.84 (d, 2H), 2.83-2.73 (t, 2 H), 2.54-2.47 (t, 2 H), 1.27 (s, 9 H). ^{13}C-NMR (DMSO-d_6, 100 MHz): 153.73, 135.32, 128.76, 124.42, 78.58, 36.22, 30.27, 28.92. HRMS m/z: $[M+H]^+$ calcd. for $C_{13}H_{17}O_3$: 221.1178; found 221.1167. LC-MS: t= 2.02min, m/z: 221.01 $[M+H]^+$.

Synthesis of 2

N, N'-Dicyclohexylcarbodiimide (34.81 mg, 0.169 mmol, 1 equiv) was added to a solution of **10** (37.46 mg, 0.169 mmol) in dry CH_2Cl_2 (10mL) and reacted for 30 min at RT. N-Hydroxysuccinimide (19.45 mg, 0.169 mmol) was added to the reaction and further reacted overnight at RT. The mixture was filtered and concentrated to obtain a white NHS-activated product without further purification. In another flask, **9** (50 mg, 0.028 mmol) was dissolved in TFA/CH_2Cl_2 (2 mL, 1/1, v/v) and stirred at RT for 40 min before removing TFA by a gentle stream of nitrogen. Dry DMF (10 mL) and DIPEA (24.38 µL, 0.14 mmol) were added to the intermediate and stirred for 20 min. Subsequently, the NHS-activated product was added to the reaction and the mixture was stirred at RT overnight. Afterward, the mixture was flushed with nitrogen, followed by adding TFA/CH_2Cl_2 (5 mL, 1/1, v/v) and stirring for 2 hours. The crude was concentrated and purified on silica column chromatography (EtOAc/CH_3OH-CH_2Cl_2/CH_3OH,

100/00-80/20, v/v) to obtain a brownish oil. The compound was further purified by HPLC with UV detection and lyophilized to harvest the white solid compound.

Yield: 42.9%, 23.01 mg. ^{1}H-NMR (DMSO-d_6, 400 MHz): 9.47-8.68 (br s, 3H), 8.33-8.29 (s, 1H), 7.94-7.80 (t, 3H), 7.75-7.25 (br d, 6H), 7.22-7,12 (m, 3H), 7.00-6.91 (m, 6H), 6.67-6.56 (m, 6H), 4.08-3.96 (t, 6H), 3.62-3.30 (m, 54H), 3.21-3.12 (m, 6H), 2.35-2.22 (t, 6H), 2.98-2.88 (m, 6H), 2.71-2.61 (t, 6H), 1.56-1.32 (m, 12H), 1.32-1.09 (m, 24H); ^{13}C-NMR (DMSO-d_6, 100 MHz): 182.90, 172.10, 156.65, 155.91, 148.12, 131.87, 129.14, 115.19, 70.26, 70.23, 70.07, 69.66, 69.41, 63.49, 40.70, 38.98, 37.94, 31.19, 30.84, 29.90, 29.19, 29.13, 26.74, 26.36. HRMS (ESI) m/z: $[M+H]^+$ calcd. for $C_{96}H_{148}N_{13}O_{27}$: 1916.30345; found: 1916.06335. LC-MS: t= 6.05 min, m/z 1915.33 $[M]^+$.

PEG-4Phe

N, N'-Dicyclohexylcarbodiimide (DCC) (0.83 g, 4.0 mmol) was added dropwise into a stirring solution of 3-(4-(tert-butoxy)phenyl)propanoic acid (0.88 g, 4.0 mmol) in CH_2Cl_2 (10 mL) at RT. A white precipitate was immediately observed after the DCC addition. 4arm-PEG-OH (Mw: 10 kDa) (2.0 g, 0.2 mmol), pyridine (129.2 µL, 1.6 mmol) and DMAP (0.024 g, 0.2 mmol) were stirred at RT in CH_2Cl_2 (10 mL) in another flask separately. After 30 min stirring, the two solutions were combined, and the mixture was further reacted overnight at RT. Afterward, the mixture was filtered, and concentrated by rotary evaporation before being precipitated in cold diethyl ether, washed and re-dissolved in CH_2Cl_2. The precipitation step was repeated three times. The obtained concentrated liquid was then reacted with 50% TFA in CH_2Cl_2(v/v) overnight. The reacted solution was concentrated by a stream of nitrogen gas and removed TFA, re-dissolved in Milli-Q water, dialyzed for three days, and lyophilized overnight to obtain a white solid. Yield: 1.75 g, 87.5%. ^{1}H-NMR ($CDCl_3$, 400 MHz): 7.07-6.98 (d, 8H), 6.82-6.74 (d, 8H), 4.26-4.16 (d, 8H), 3.89-3.34 (m, 904H), 2.92-2.80 (t, 8H), 2.68-2.54 (t, 8H).

The degree of phenol group functionalization was confirmed by ^{1}H-NMR ($CDCl_3$, 400 MHz) using the integral ratio of the alkene protons on the PEG adjacent to ester bond (4.26-4.16 ppm, 7.42H), to that of actual value for complete conversion (4.26-4.16 ppm, 8H), which was found to be around 92.8%. The protons (3.89-3.34 ppm, 226H) were used for calibration.

Hybrid hydrogel preparation and gel inversion experiments

Stock solutions of C8-SQ (10 mM) and SQ-Phe (10 mM) were prepared separately by dissolving the monomers in DMSO with 3 min vortexing. Aliquots of C8-SQ (10 mM) and SQ-Phe (10 mM) were mixed at different ratios as needed. For example, to prepare C8-SQ/5SQ-Phe (with the total monomer concentration containing 5 mol% SQ-Phe) hydrogels at the required concentration and volume, C8-SQ (83.6 µL, 10 mM) and SQ-Phe (4.4 µL, 10 mM) stock solutions were pipetted into the glass vials (2.0 mL) with 1 min of gentle vortexing to obtain the C8-SQ/5SQ-Phe (8.8 mM, 100 µL) hydrogel. Subsequently, the solutions were dried overnight under a stream of nitrogen gas to obtain dried films. PBS (pH 7.4, 100 µL) was added to the films of supramolecular monomers and sonication was performed in an ice bath (~4 °C) yielding a clear solution. The sample was kept on ice until further usage. To prepare the **DN1-6** hydrogels, a stock solution of PEG-4Phe (10 wt %) was prepared in PBS (pH 7.4). The C8-SQ/5SQ-Phe (8.8 mM) hydrogel and PEG-4Phe (10%) were mixed after calculation to obtain the determined hydrogels. For example, to prepare **DN1** hydrogel (100 µL without photoinitiators), 22.7 µL of C8-

SQ/5SQ-Phe (8.8 mM) hydrogel, 10 µL of PEG-4Phe (10 wt %) and 57.3 µL PBS were mixed within the vail for further usage.

All the samples were left to equilibrate overnight before further use. Photoinitiator tris(bipyridine)ruthenium(II) chloride (Ru, 44 mM) and sodium persulfate (SPS, 440 mM) were prepared separately. Pre-determined volumes of Ru and SPS stock solutions were added into prepared gels and gently pipetted 10 times to evenly mix them before use. For example, for a 100 µL volume of the **DN** hydrogel, 1.25 µL of Ru (44 mM), 1.25 µL of SPS (440 mM) and 7.5 µL of PBS were added for **DN1-3**, 1.63 µL of Ru (44 mM), 1.63 µL of SPS (440 mM) and 6.74 µL of PBS for **DN4-6** were added. The mixture was pipetted gently to mix well prior to visible light-mediated crosslinking of the gels.

The critical gelation concentration (CGC) was defined as the minimum concentration of a given compound to form a hydrogel. The CGC of **PN** and **DN** hydrogels was determined by the gel inversion method. **PN1-2** and **DN1-6** hydrogels were prepared with PBS in 2 mL glass vials as described above. Digital photos of the inverted vials containing gels were taken before crosslinking, after crosslinking by irradiating with visible light for 2 min using a benchtop LED source (~10 mW/cm^2, 450 nm) and after incubating in 37^{o}C oven for 28 days (Figure S1-2).

Hydrogel Swelling Performance and Gel Stability Test

Hydrogel swelling ratios were measured after crosslinking and swollen for 24 h until a constant weight was reached. Gel stability data was acquired by weighing hydrogels at different time points. Hydrogels were prepared with PBS (100 µL) as described before in 2 mL glass vials, equilibrated overnight, prior to crosslinking with photoinitiators for 2 min by using a benchtop LED (λ=450 nm, ~ 10 mW/cm^2). The hydrogels were covered with PBS (300 µL) and kept at 37^{o}C in an oven for 4 weeks. Digital photos were obtained before crosslinking, after crosslinking and 28 days after maintenance in PBS at 37^{o}C. The weight was recorded at different time points as W*wet*. Hydrogels' W*equ* were recorded until the constant weight of hydrogels was reached. After 15 days, the hydrogels were lyophilized, and the dried products were weighed as W*dry*. Hydrogel swelling ratios were calculated using the formula: $Swelling\ Ratio = (Wequ - Wdry)/Wdry$. Gel stability was calculated using the formula: $Gel\ erosion\% = 100 \times (Wwet - Wdry)/Wequ$. Each condition was performed in triplicate.

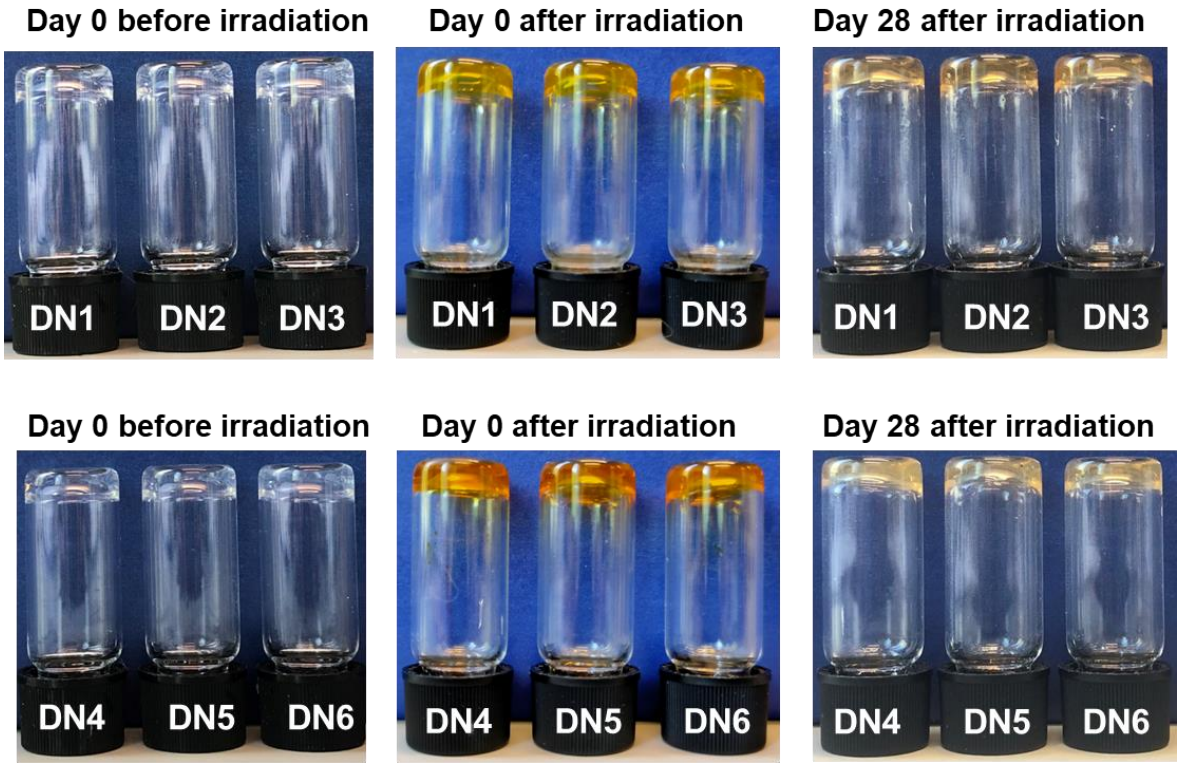

Figure S2. Gels inversion experiments of **DN1-6** hydrogels after 2 min visible light irradiation using a benchtop of LED.

Oscillatory rheology study

The prepared hydrogels (**SN**, **IPN1-2**, **DN1-6**) (45 µL) and **PN1-2** solutions (42 µL) prior to photocorsslinking were gently pipetted onto the quartz plate of the rheometer. The upper plate was then lowered to a gap distance of 500 µm. The loaded samples were equilibrated for 5 min before data collection and the samples were then exposed to visible light for 3 min. Time sweeps (frequency = 1.0 Hz, strain = 0.05%), frequency sweeps from 0.01 to 10 Hz (strain = 0.05%), and strain sweeps from 0.01 to 2000% (frequency = 1.0 Hz) were collected.

The stress relaxation behaviour of photocrosslinked hydrogels was measured at a constant strain of 10%. The creep and recovery behavior of photocrosslinked hydrogels were performed after a time sweep of 600 s with a fixed strain (0.01%) and frequency (1.0 Hz). The strain in response to a constant stress (300 Pa) was measured for 3600 s, after which the stress was removed, and the strain was measured for another 10,000 s. PBS was carefully added surrounding the hydrogels to prevent the drying process.

Table S1. Plateau storage moduli of the various hydrogels (**SN**, **PN1-2**, **IPN1-2** and **DN1-6**) with different compositions (e.g., supramolecular monomer concentration, SQ-Phe mol% in **SN**, total polymer concentration) and visible light exposure times. Averaged storage moduli are presented (N ≥ 3).

Sample name	Composition				Visible light exposure time (min)	Storage modulus before visible light exposure (Pa)	Storage modulus after visible light exposure (Pa)
	SN (mM)	**SQ** (mol%)	**SQ-Phe** (mol%)	**PEG** (wt%)			
SN	6	95	5	0	3	10 ± 4	3861 ± 698
PN1	0	0	0	1	10	S	1286 ± 198
PN2	0	0	0	2	10	S	2132 ± 259
IPN1	6	100	0	1	10	8 + 5	3858 ± 341
IPN2	6	100	0	2	3	8 + 4	9054 ± 293
DN1	2	95	5	1	3	5 ± 3	10306 ± 1563
DN2	4	95	5	1	3	6 ± 4	16083 ± 3216
DN3	6	95	5	1	3	10 ± 8	22873 ± 7465
DN4	2	95	5	2	3	5 ± 4	15031 ± 2234
DN5	4	95	5	2	3	6 ± 5	21902 ± 3978
DN6	6	95	5	2	3	11 ± 7	31956 ± 3233

[S]: Solution.

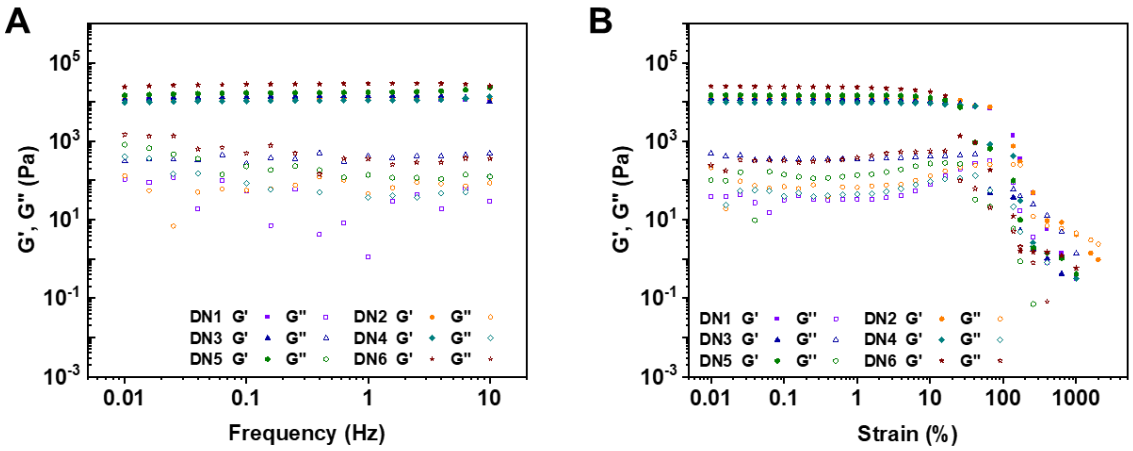

Figure S3. Averaged (N = 3) (A) frequency (0.1-10 Hz) and (B) strain (0.01-2000%) sweeps of **DN1** - **DN6** hydrogels after 3 min visible light irradiation at RT. The frequency sweep experiment was performed at a fixed strain (0.05%), and the strain experiment was collected at a constant frequency (1.0 Hz).

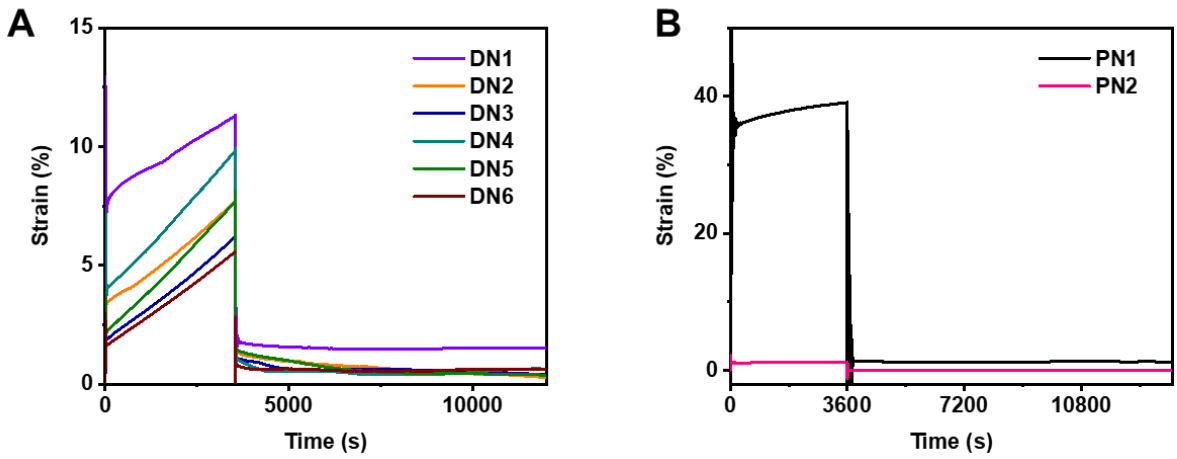

Figure S4. Creep and recovery test of (A) **DN1-6** and (B) **PN1-2** after photocrosslinking. A constant stress of 500 Pa was applied to the **DN1-6** samples and 50 Pa was applied to the **PN1-2** samples.

Compression test

The prepared samples before photocrosslinking (75 µL) were gently pipetted onto the quartz plate of the rheometer and the upper plate was lowered to 1.2 mm. The samples were equilibrated for 5 min before data collection. After a time sweep experiment of 60 s, the samples were photocrosslinked for 3 min to reach a plateau in storage modulus. PBS was carefully placed around the samples immediately after the samples were fully crosslinked to prevent evaporation during the measuring period. Afterward, an axial compression test was set up to compress the sample ~80 % of its initial height (0.2 mm gap) at different rates (100-0.1 µm/s). The compression modulus was calculated from the slope of the linear region of the compressive stress-strain curve (**SN**: strain = 0-1.35%, **PN**; **IPN** and **DN**: strain = 0-5%). Energy dissipation was probed on the photocrosslinked hydrogels by cyclic compression tests with an increasing strain percentage from 10% to 80% at a rate of 10 µm/s and then removing the load. The compression cycle was started immediately again after the release of the load. Compressive stress relaxation tests on the photocrosslinked hydrogels were performed starting with applying 10% strain to the sample at a rate of 100 µm/s. The hydrogels were compressed for 600 s at this strain percentage and stress relaxation was monitored. Steps of 10% strain were then applied to the material in sequence for the same amount of time until a maximum of 80% strain was achieved. The curves were plotted until the hydrogel was fractured. Poroviscoelastic relaxation tests on photocrosslinked hydrogels were measured by applying a 15% consistent strain at a rate of 150 µm/s, and the stress relaxation was monitored for another 10 000s. A two-term exponential decay model was used to fit the load-log(t) graphs at a compressive strain of 15% to obtain time constants[3,4]:

$$y = y_0 + Ae^{-\left(\frac{t}{\tau_1}\right)} + Be^{-C\left(\frac{t}{\tau_2}\right)^D}$$

Here, y_0 represents the load value (kPa) after complete stress-relaxation, t indicates the time during the pause phase (s), A and B are coefficients related to y_0 (kPa). Additionally, C and D are coefficients correlated to geometric compression and the strain limit, while τ_1 and τ_2 signify characteristic short-term and long-term stress-relaxation time scales, respectively. These six fitting

parameters (A, B, C, D, τ_1, and τ_2) were determined using a built-in nonlinear curve fitting tool in Origin (OriginLab Corporation) for stress-relaxation curve fitting. The time was set to 0s when the strain reached 15% and the maximum stress value obtained. The accuracy of the least-squares fitting algorithm was evaluated using residual plots, residual sum of squares, and adjusted R^2 values. The comparison to global minima was based on the sum of squared errors between the actual data points and the best-fit curve.

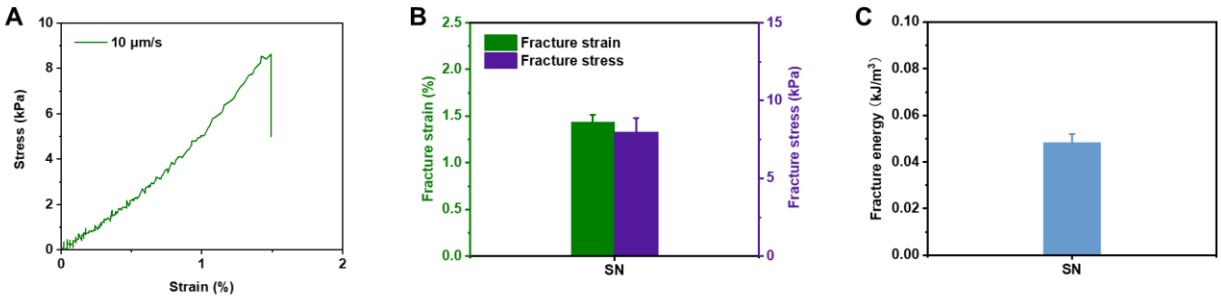

Figure S5. Mechanical properties of **SN** hydrogel: (A) Uniaxial stress-strain curves of **SN** at a 10 μm/s compression speed. (B) Compressive fracture strain, fracture stress **SN** hydrogel. (F) Fracture energy of **SN** hydrogel. Mean ± SD, N ≥ 3.

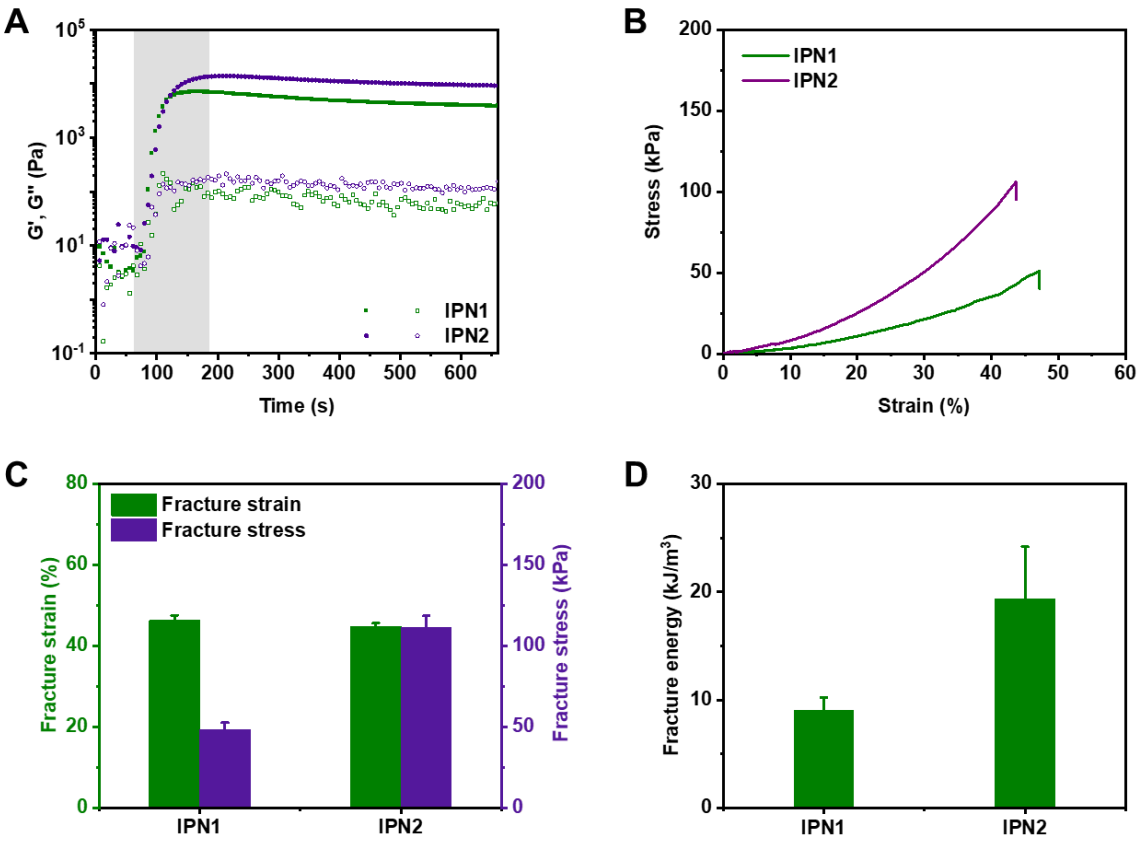

Figure S6. Mechanical properties of **IPN1-2** hydrogels: (A) Time sweep experiment after 3 min visible light exposure. Grey regions indicate visible light exposure. (B) Uniaxial stress-strain curves of **IPN1-2** hydrogels at 10 μm/s compression speed.

(C) Compressive fracture strain, fracture stress of **IPN1-2** hydrogels. (F) Fracture energy of **IPN1-2** hydrogels. Mean ± SD, N ≥ 3.

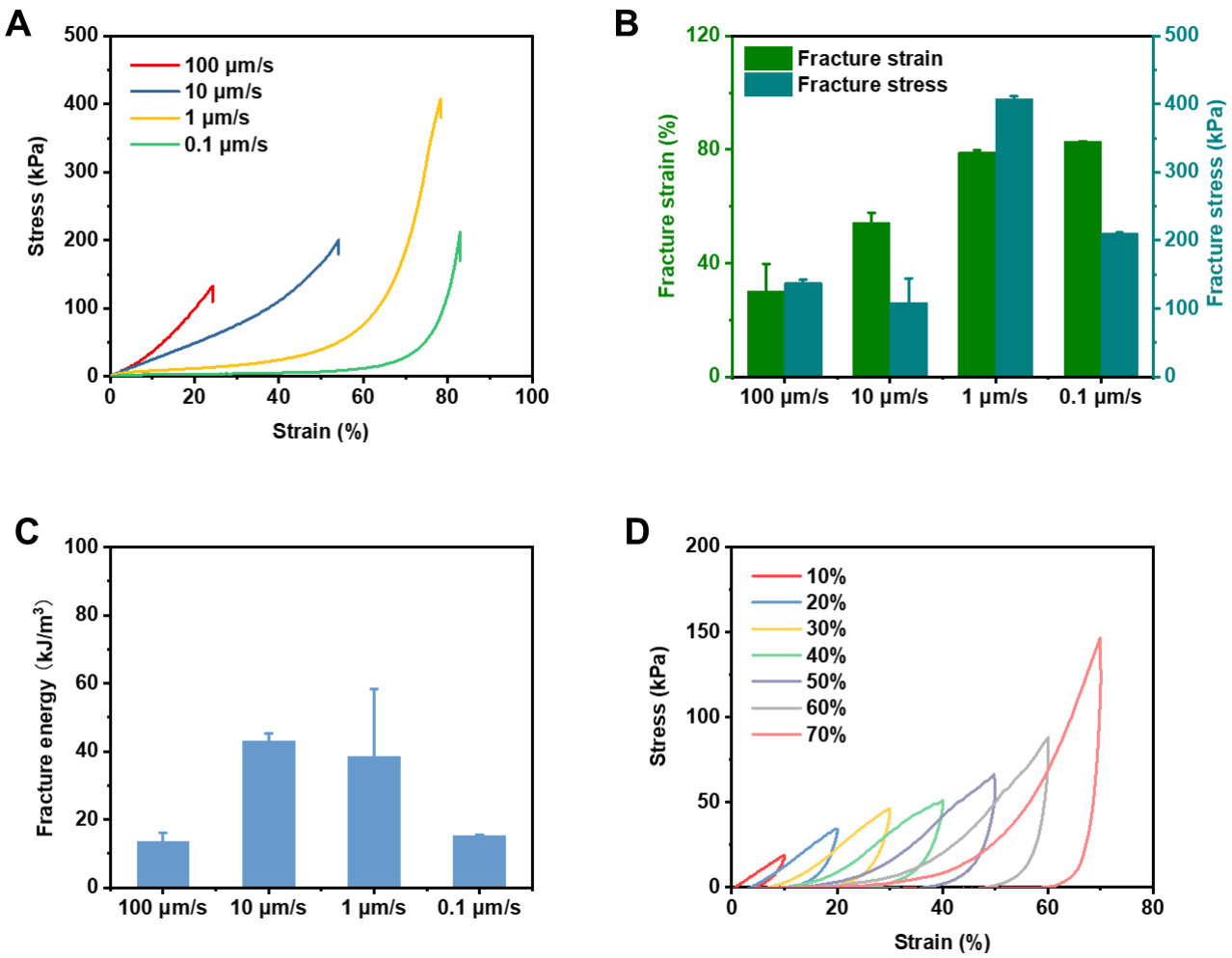

Figure S7. Mechanical properties of **DN1** hydrogel: (A) Uniaxial stress-strain curves at different compression speeds. (B) Compressive fracture strain, and fracture stress at different compression speeds. (C) Fracture energy at different compression speeds. (D) Step-stress relaxation curves with increasing strain (10%) at the start of each loading cycle. Mean ± SD, N ≥ 3.

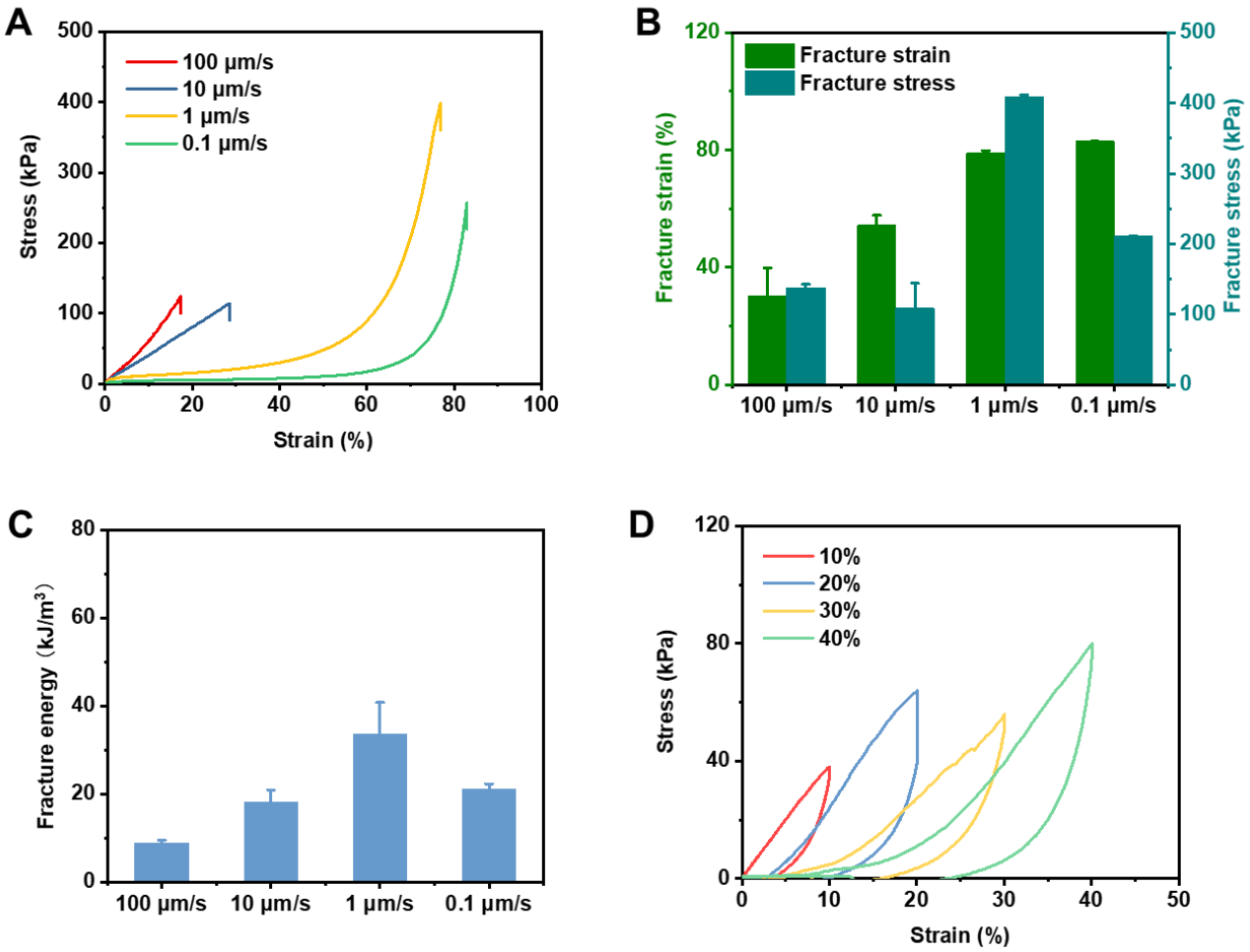

Figure S8. Mechanical properties of **DN2** hydrogel: (A) Uniaxial stress-strain curves at different compression speeds. (B) Compressive fracture strain, and fracture stress at different compression speeds. (C) Fracture energy at different compression speeds. (D) Step-stress relaxation curves with increasing strain (10%) at the start of each loading cycle. Mean ± SD, N ≥ 3.

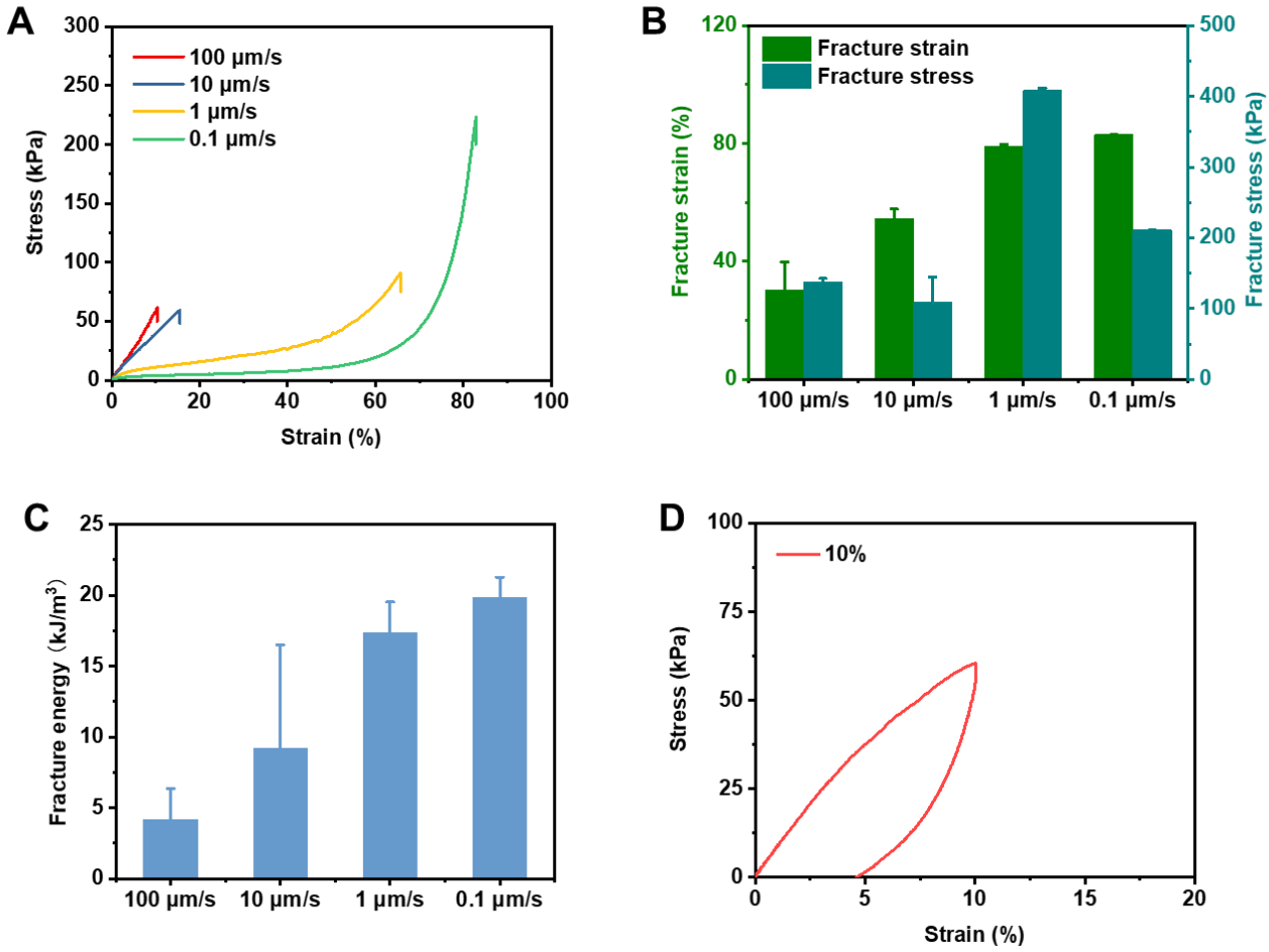

Figure S9. Mechanical properties of **DN3** hydrogel: (A) Uniaxial stress-strain curves at different compression speeds. (B) Compressive fracture strain, and fracture stress at different compression speeds. (C) Fracture energy at different compression speeds. (D) Step-stress relaxation curves with increasing strain (10%) at the start of each loading cycle. Mean ± SD, N ≥ 3.

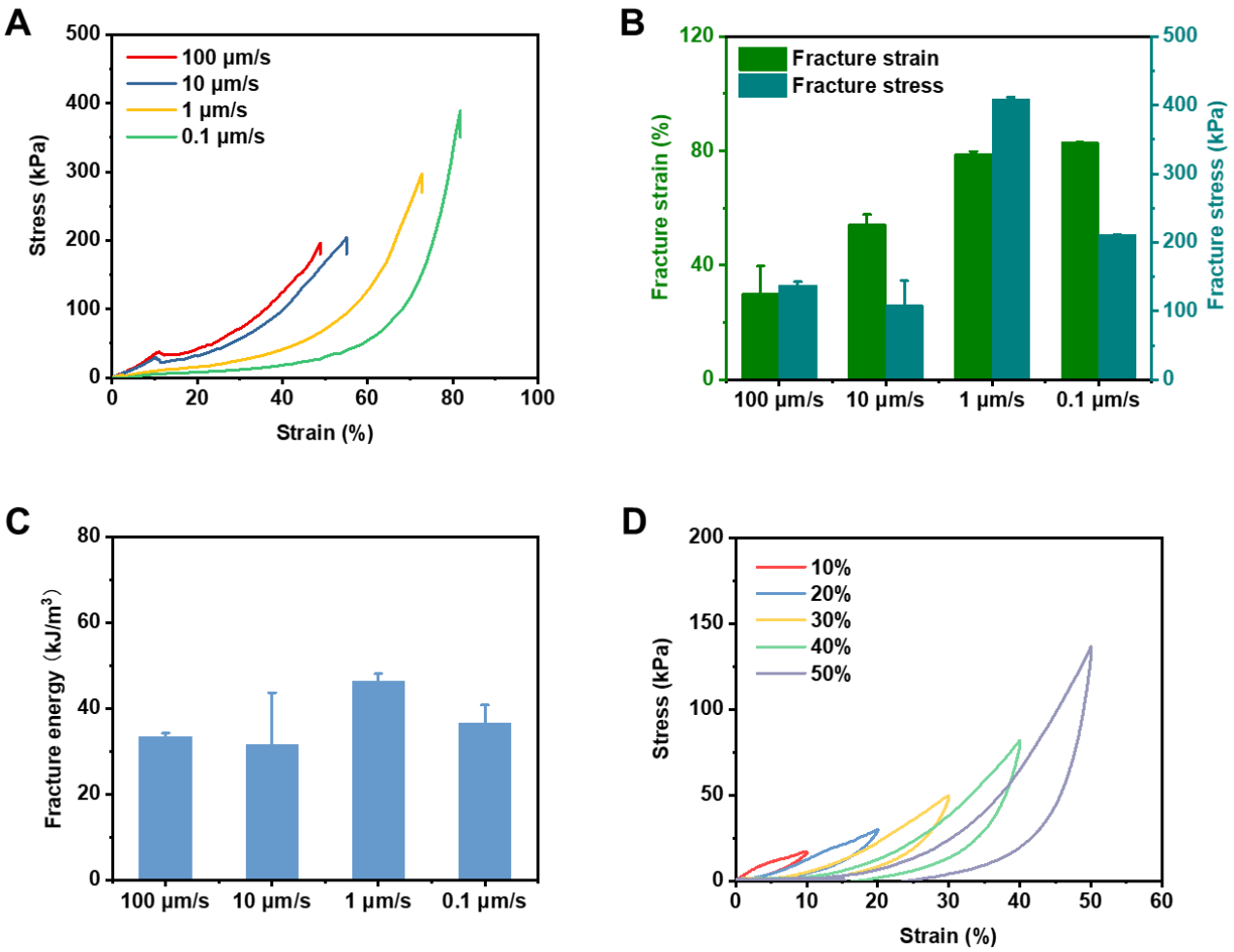

Figure S10. Mechanical properties of **DN4** hydrogel: (A) Uniaxial stress-strain curves at different compression speeds. (B) Compressive fracture strain, and fracture stress at different compression speeds. (C) Fracture energy at different compression speeds. (D) Step-stress relaxation curves with increasing strain (10%) at the start of each loading cycle. Mean ± SD, N ≥ 3.

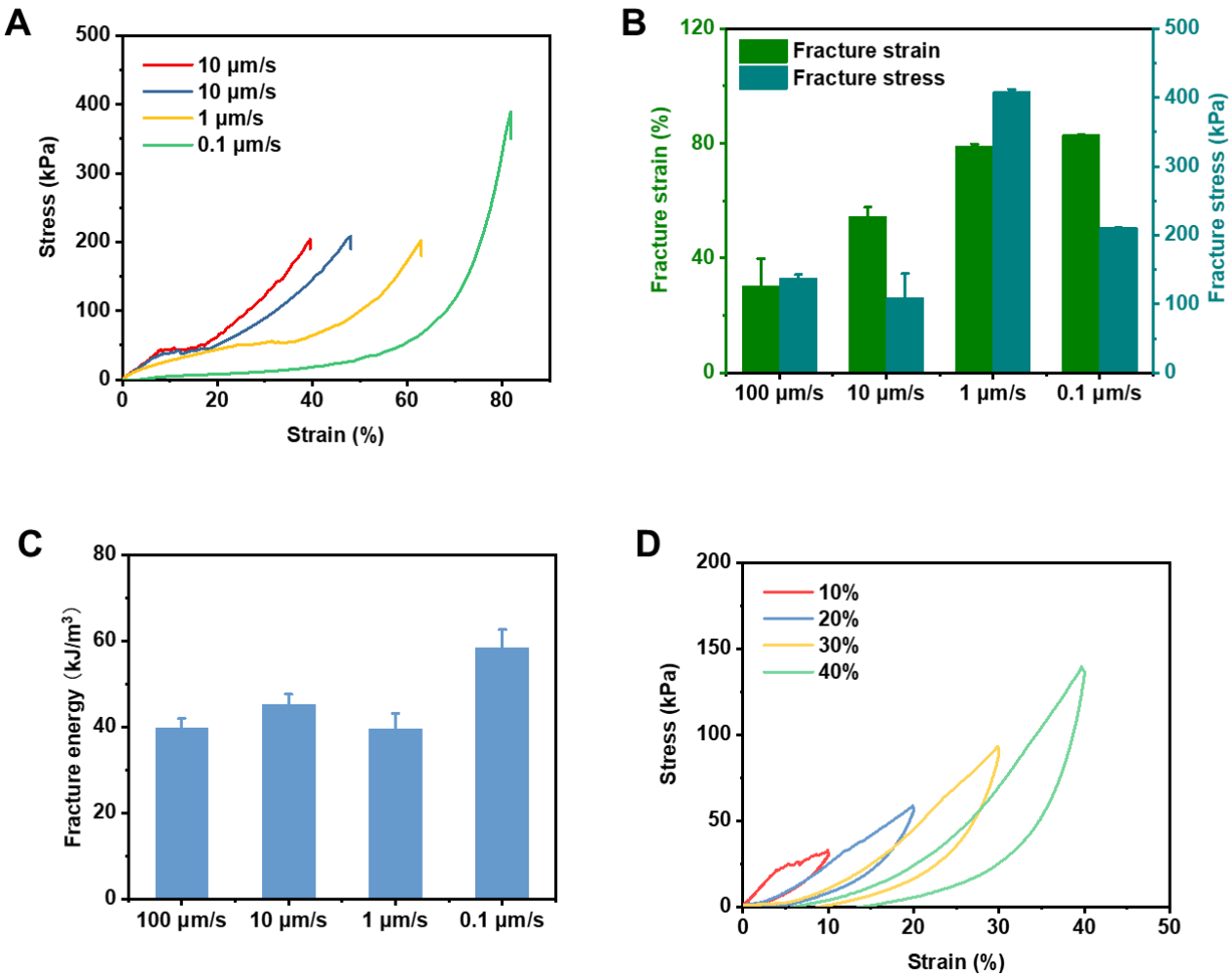

Figure S11. Mechanical properties of **DN5** hydrogel: (A) Uniaxial stress-strain curves at different compression speeds. (B) Compressive fracture strain, and fracture stress at different compression speeds. (C) Fracture energy at different compression speeds. (D) Step-stress relaxation curves with increasing strain (10%) at the start of each loading cycle. Mean ± SD, N ≥ 3.

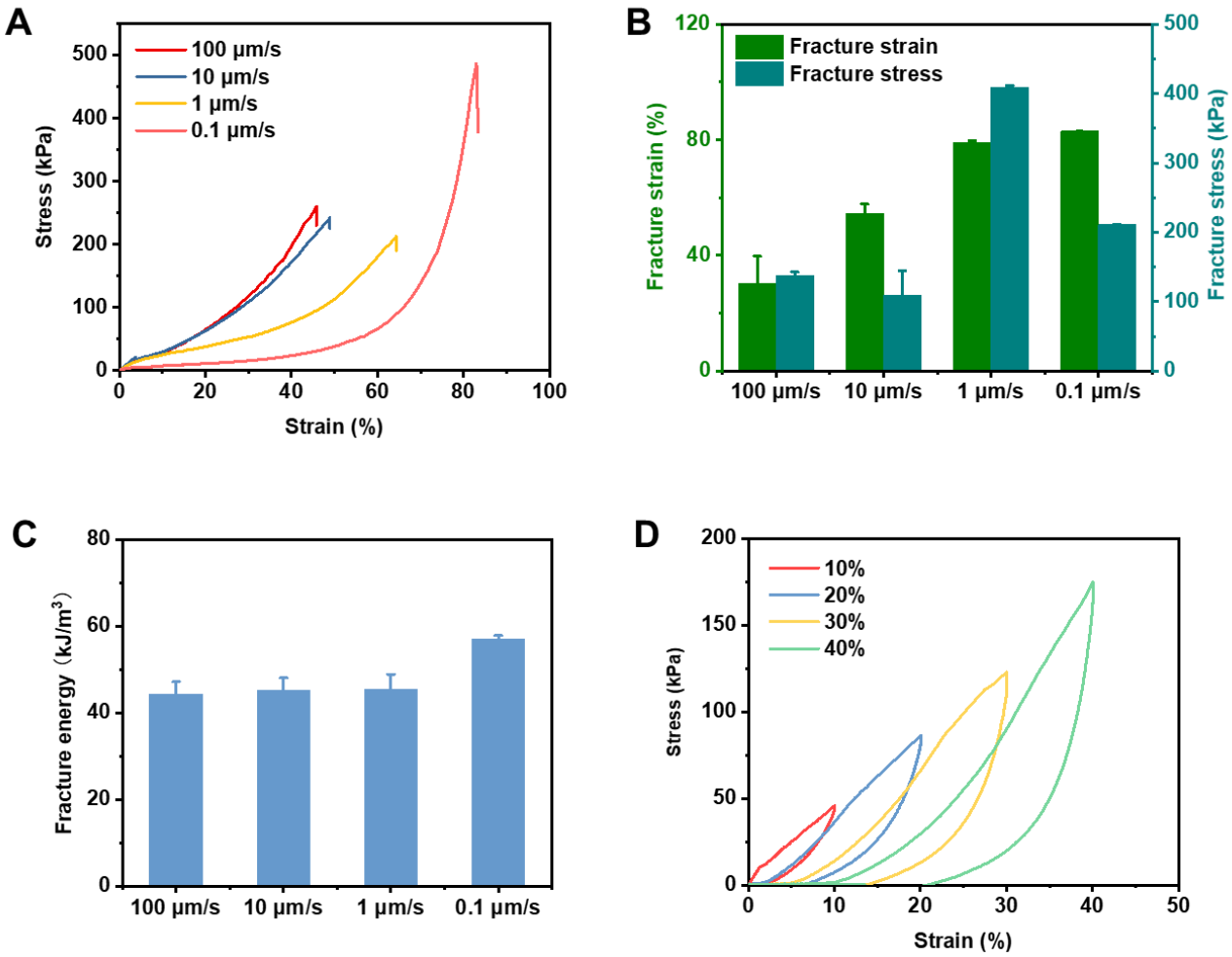

Figure S12. Mechanical properties of **DN6** hydrogel: (A) Uniaxial stress-strain curves at different compression speeds. (B) Compressive fracture strain, and fracture stress at different compression speeds. (C) Fracture energy at different compression speeds. (D) Step-stress relaxation curves with increasing strain (10%) at the start of each loading cycle. Mean ± SD, N ≥ 3.

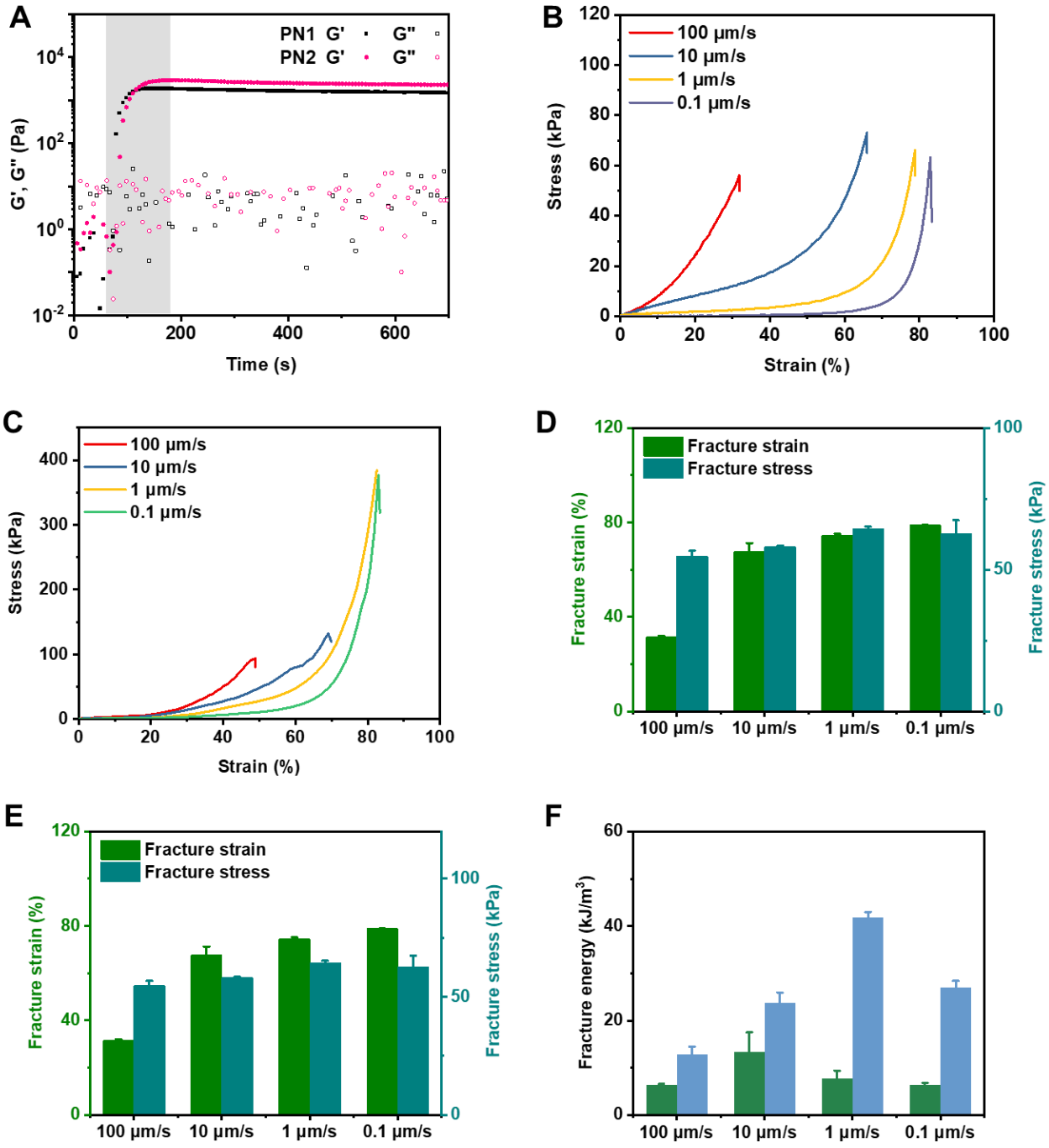

Figure S13. Mechanical properties of **PN1-2** hydrogels: (A) Time sweep experiment after 3 min visible light exposure. Uniaxial stress-strain curves of (B) **PN1** and (C) **PN2** at different compression speeds. Compressive fracture strain, fracture stress of (D) **PN1** and (E) **PN2** hydrogel. (F) Fracture energy of **PN1-2** hydrogels. Mean ± SD, N ≥ 3.

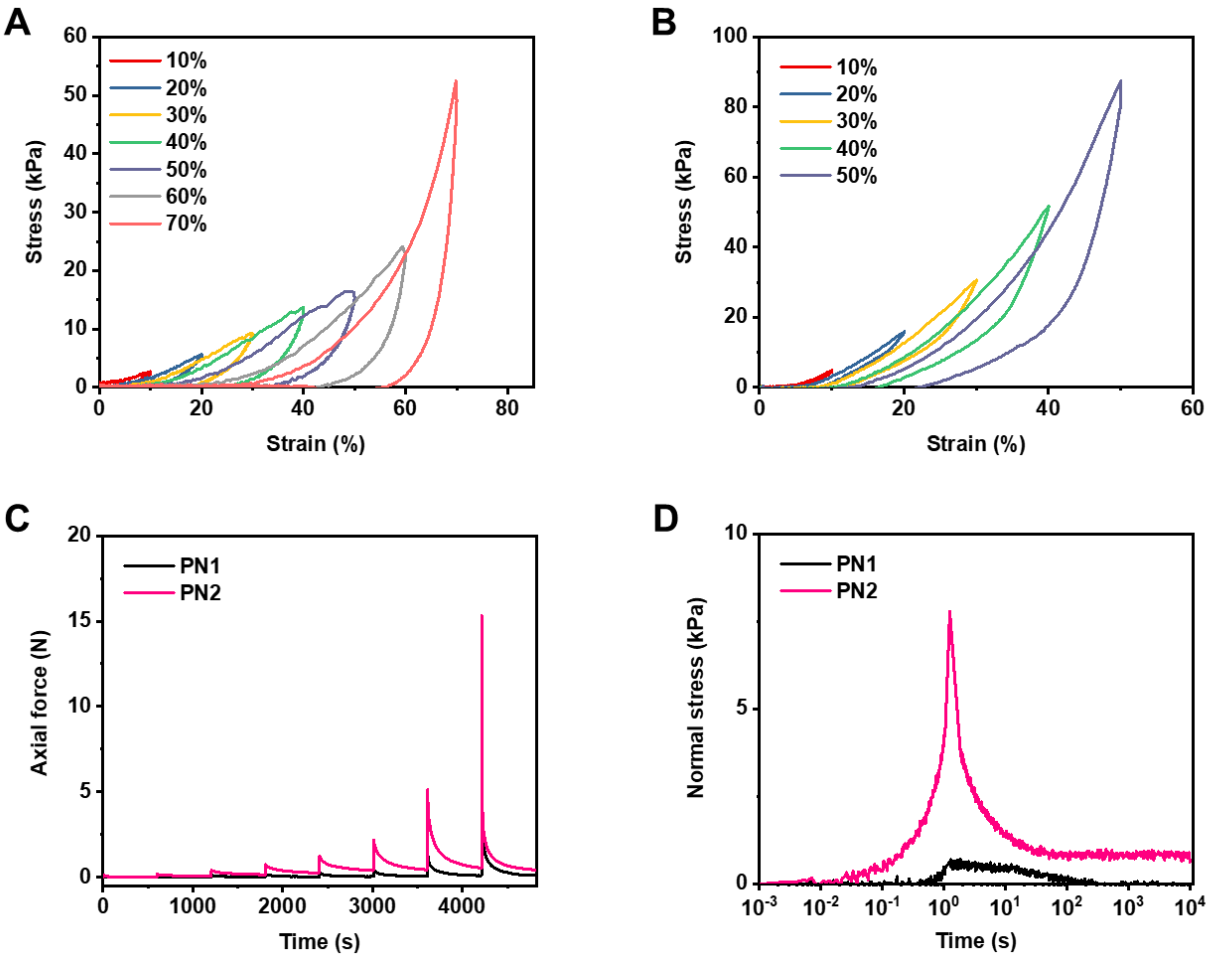

Figure S14. Uniaxial compression cycles of (A) **PN1** and (B) **PN2** hydrogels at different maximum strains. (C) Step-stress relaxation curves with increasing strain (10%) at the start of each loading cycle. (D) Poroviscoelastic relaxation curves of **PN1** and **PN2** hydrogel under a 15% instant strain.

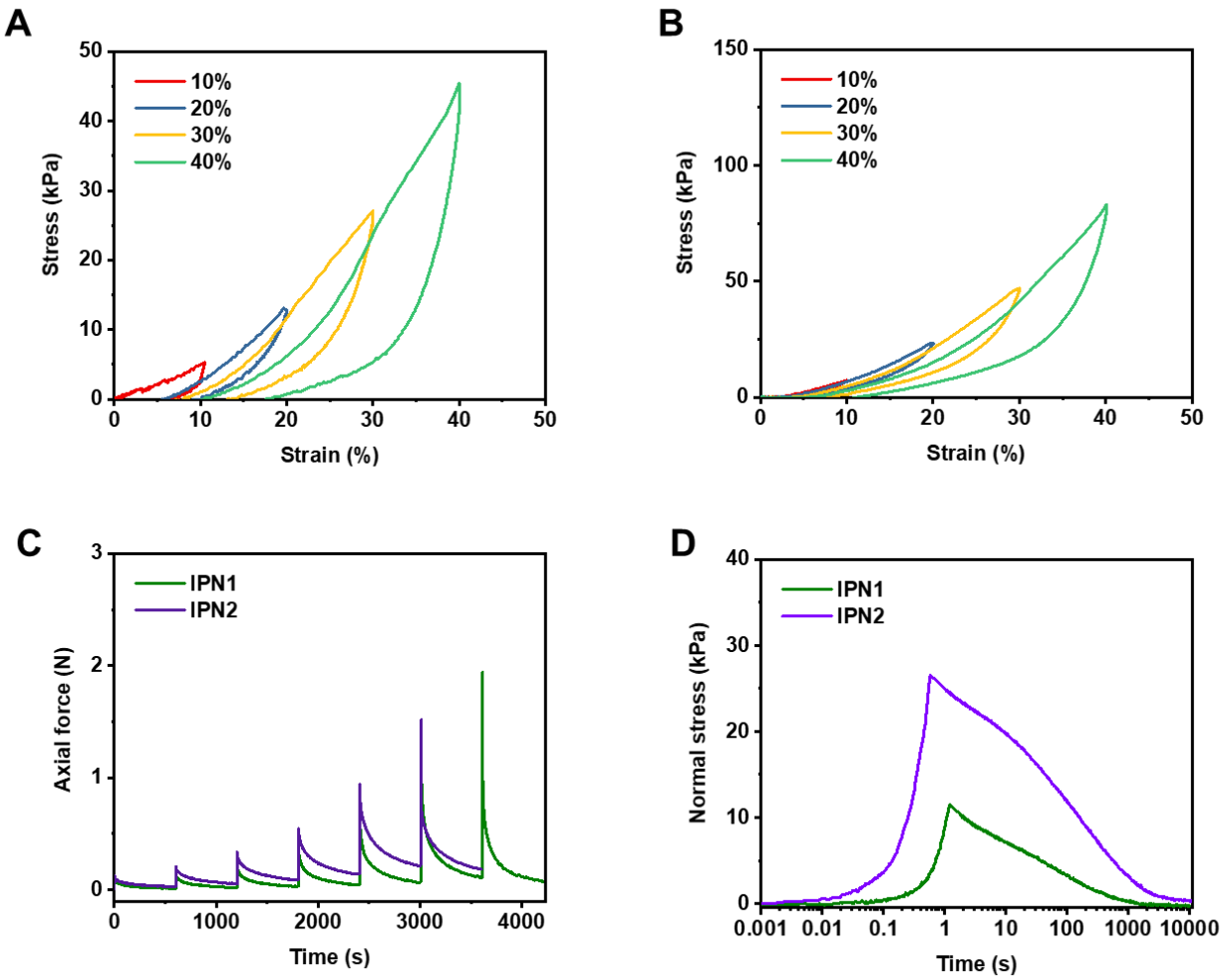

Figure S15. Uniaxial compression cycles of (A) **IPN1** and (B) **IPN2** hydrogels at different maximum strains. (C) Step-stress relaxation curves with increasing strain (10%) at the start of each loading cycle. (D) Poroviscoelastic relaxation curves of **IPN1** and **IPN2** hydrogel under a 15% instant strain.

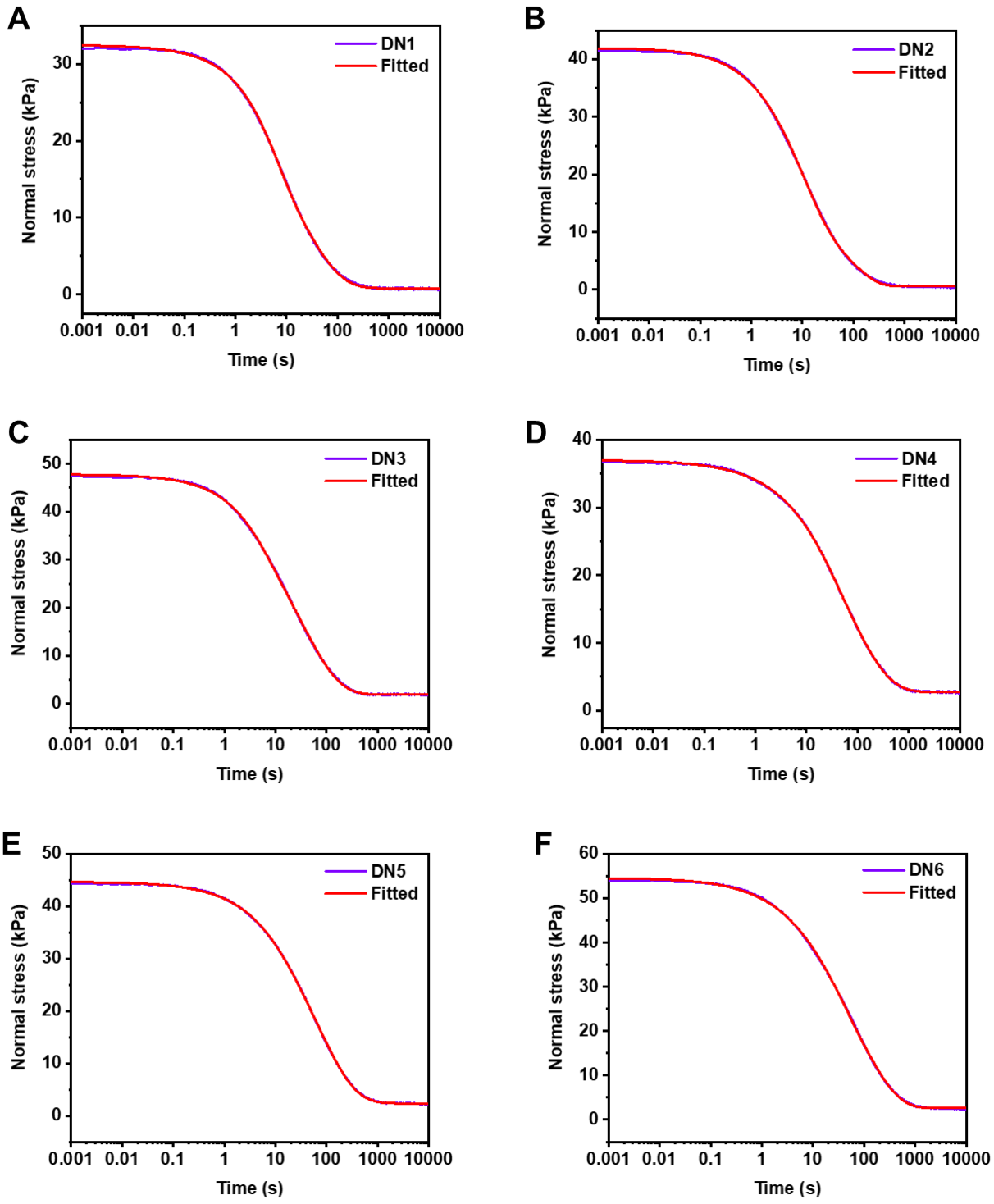

Figure S16. Fitting of the poroviscoelastic data to a two-term exponential decay model for the following hydrogels: (A) **DN1**, (B) **DN2**, (C) **DN3**, (D) **DN4**, (E) **DN5**, (F) **DN6**. R^2= 0.9958-0.9996.

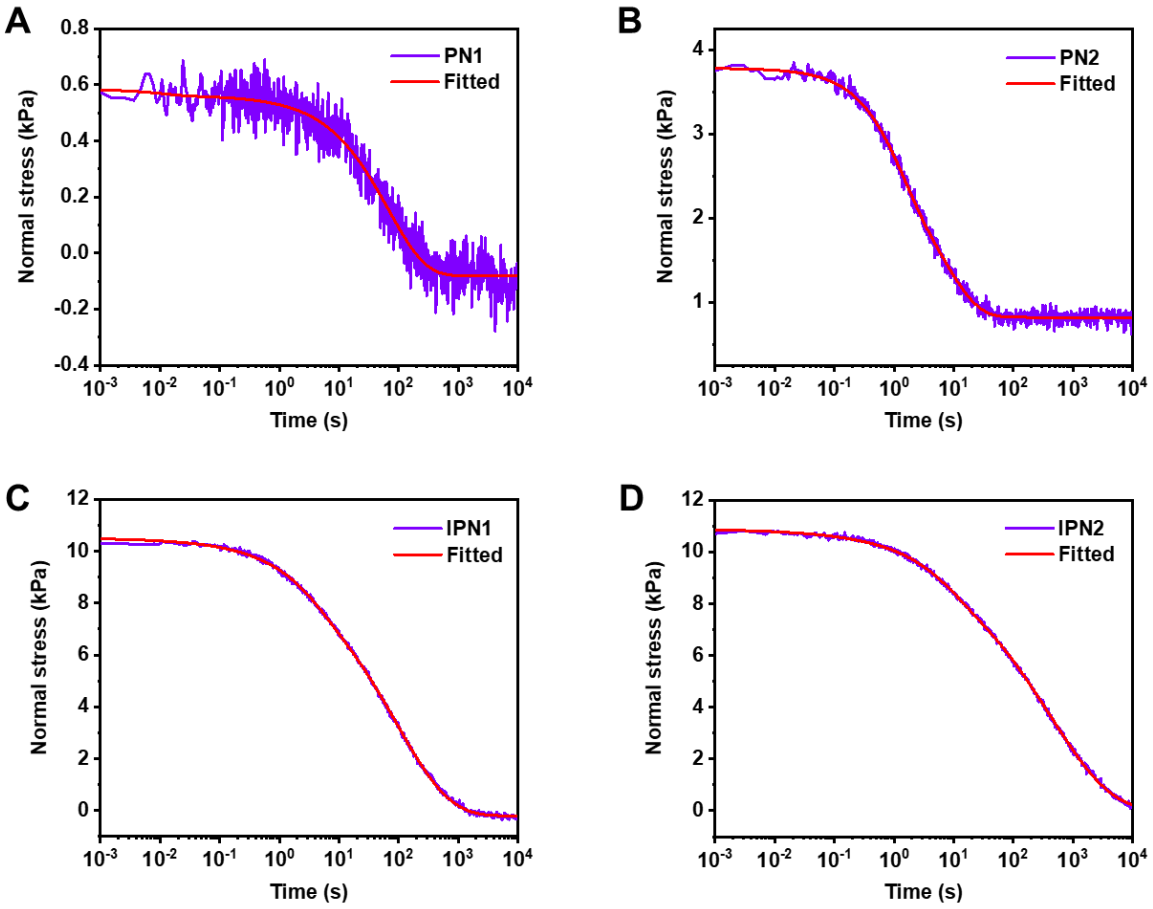

Figure S17. Fitting of the poroviscoelastic data to a two-term exponential decay model for the following hydrogels: (A) **PN1**, (B) **PN2**, (C) **IPN1**, (D) **IPN2**. R^2= 0.95363-0.9997.

Table S2. Fitting results of poroviscoelastic relaxation of different hydrogels.

	τ_1 (s)	τ_2 (s)	R^2
DN1	6.1083 ± 0.08444	1795.79775 ± 7233.36181	0.99952
DN2	5.74067 ± 3.16338	573.74555 ± 73.98957	0.99992
DN3	5.26353 ± 0.12849	175.56259 ± 422.43425	0.99992
DN4	24.50284 ± 0.9517	30.46237 ± 80.87255	0.99989
DN5	12.99155 ± 0.63101	174.13445 ± 277.648	0.99991
DN6	6.96119 ± 0.14635	249.85593 ± 360.5069	0.99997
IPN1	3.87477 ± 0.1738	1.40823 ± 6.6273	0.9997
IPN2	8.4959 ± 0.37531	70.65463 ± 768.36301	0.99965
PN1	0.01087 ± 0.02628	73.96757 ± 2035.46098	0.95363
PN2	1.11349 ± 0.09375	778.86237 ± 13296.12861	0.9968

Scanning electron microscopy (SEM)

Hydrogels (400 µL) were prepared as described above and irradiated with visible light for 5 min by an LED source. The hydrogels were subsequently freeze-dried overnight and fractured after briefly dipping the solids in liquid nitrogen using tweezers. The fractured pieces were directly applied onto two-sided conductive tape attached to an aluminum stub and coated for 2 min by a thin layer of gold (under vacuum) before imaging. The aperture size distribution of the hydrogel was measured at least 50 apertures per sample by using Fiji software.

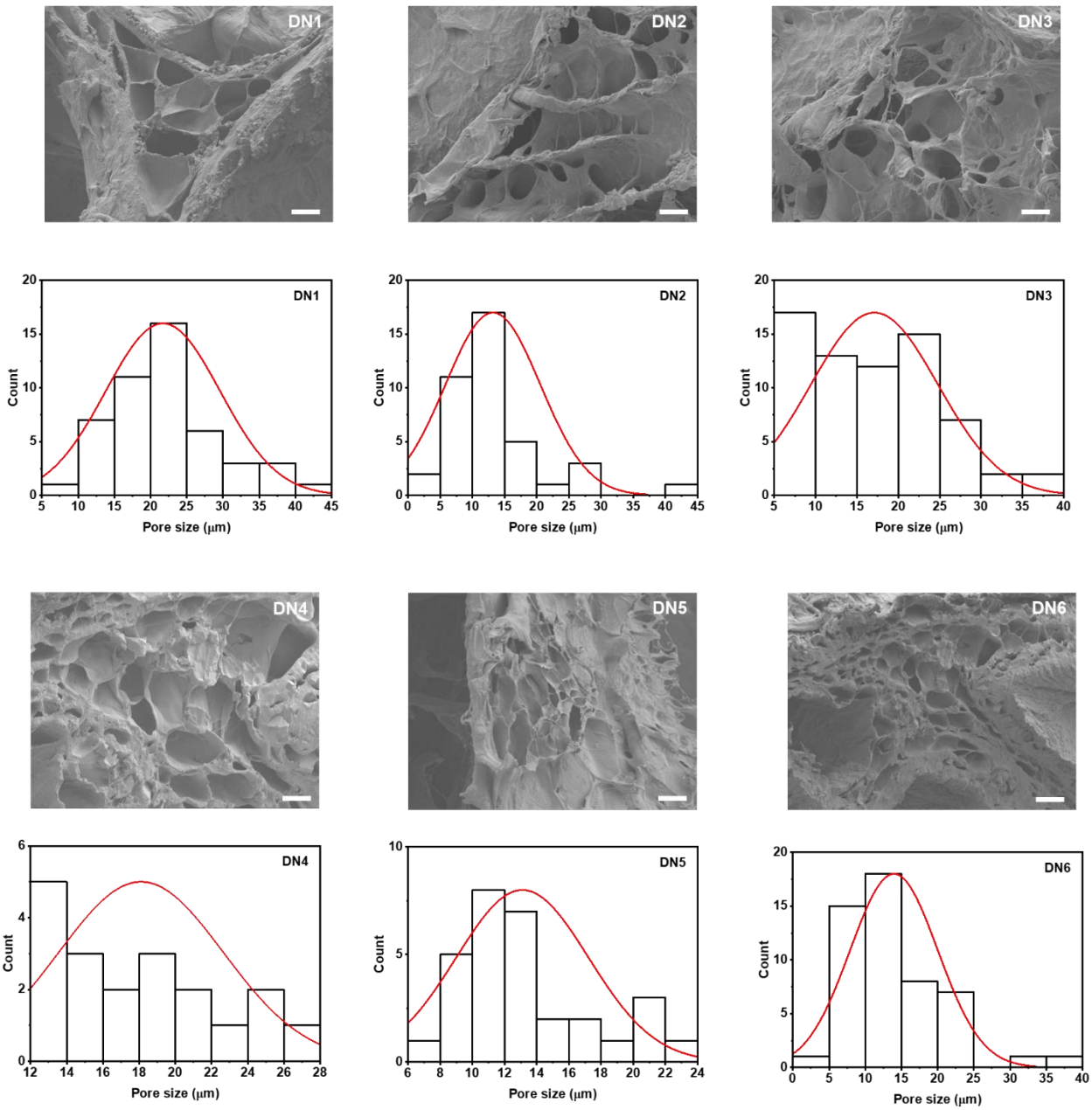

Figure S18. SEM images of various **DN1-6** hydrogels and their relative distribution of pore size. The pore size was measured from the SEM images using the Image J software. Scale bar: *20 μm*.

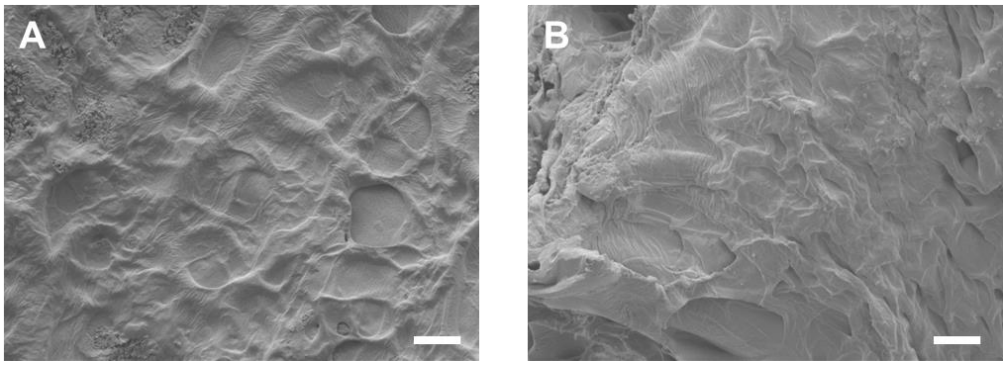

Figure S19. The cross-section SEM images of **DN** hydrogels: (A) **DN1** (B) **DN6**.

Transmission electron microscopy (TEM)

Hydrogels were prepared in PBS and equilibrated overnight as described above. The hydrogels were irradiated with visible light for 0 or 5 min. The samples with/without crosslinking were subsequently diluted with PBS to their measured concentrations (0.5 mM). Diluted solutions (15 µL) were carefully placed on a Formvar/Carbon 200 Mesh Copper grid and kept for 2 min. Afterward, uranyl acetate (1%, 10 µL) was blotted on the grid for 1 min and the grid was dried overnight at RT before imaging.

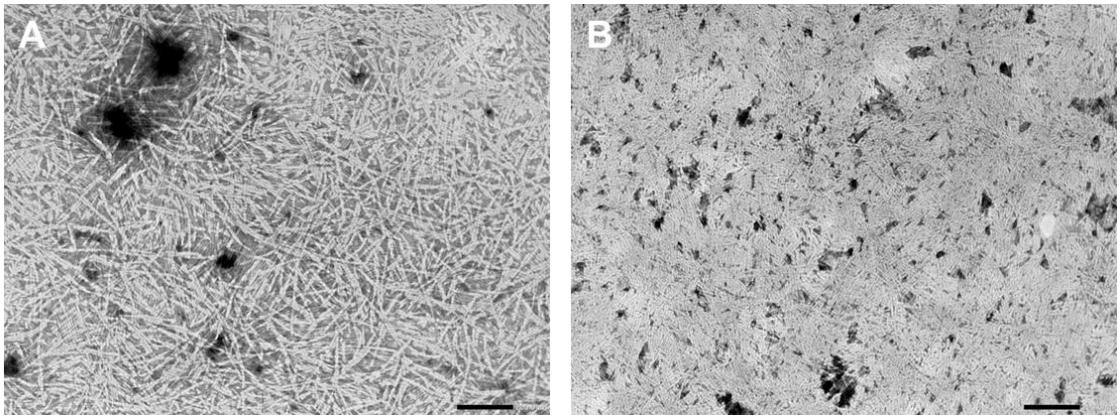

Figure 20. TEM images of diluted (A) **DN1** and (B) **DN6** after photocrosslinking. Scale bar: *200 nm*.

human primary articular chondrocytes (hPACs) culture

Collection and expansion of hPACs from the ongoing Research Arthritis and Articular Cartilage (RAAK) study were performed as earlier described.[5] In short, within 2 hours following joint replacement surgery of osteoarthritis patients, cartilage of the macroscopically unaffected (preserved) region of the joint was sampled in DMEM (high glucose) supplemented with 10% FBS, antibiotics penicillin (100 units/mL) and streptomycin (100 µg/mL) and collagenase Type I (2 mg/mL); and were incubated overnight under standard conditions. Subsequently, isolated chondrocytes were expanded for 2 passages in DMEM supplemented with 10% FBS, antibiotics (100 units/mL penicillin and 100 µg/mL streptomycin) and FGF-2 (0.5 ng/mL) prior to encapsulation into the hydrogel materials.

3D cell encapsulation and cell viability test

Cells were mixed with different **DN** hydrogels (prepared in PBS) and seeded in 15-well µ-Slide at a seeding cell density of 5 x 10^6 cells/mL. After crosslinking for 2 min by a benchtop LED, 3D constructs were covered with chondrogenic differentiation medium (50 µL) (DMEM high glucose supplemented with ascorbate (50 µg/mL), dexamethasone (0.1 µM), L-proline (40 µg/mL), sodium pyruvate (100 µg/mL), ITS-plus, antibiotics, and TGF-β1 (10 ng/mL) and cultured under standard conditions. Cell media was refreshed 3 times every 15 min after seeding and was changed daily during the experiment. The LIVE/DEAD (calcein AM/propidium iodide (PI)) assay was used to probe the cell viability after 3D encapsulation of the cells within the hydrogel. The mixed staining solutions of calcein AM (2.0 µM) and PI (1.5 µM) were prepared by diluting pre-prepared stock solutions of calcein AM (2.5 mM in DMSO) and PI (1.5 mM in PBS) with PBS (pH 7.4). After 24 h culture, the medium on top of the hydrogels was

removed before washing with PBS (2 x 50 µL). Subsequently, a mixture of staining solution (50 µL) was added to the hydrogels and the hydrogel-cell mixtures were incubated for 40 min at 37 °C without light. Subsequently, the staining solution was replaced with PBS and fixed for 30 min with a 4% paraformaldehyde (PFA) solution. Fluorescent Z-stack images were obtained using a 488 nm laser for excitation of calcein AM and a 532 nm laser for excitation of the PI dye. The Image J software package was used to process the collected raw images and count cell viability. LIVE/DEAD staining of hPACs was counted using the Fiji/ImageJ macro written for 3D analysis.

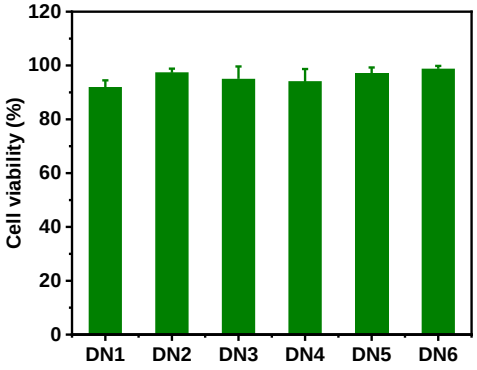

Figure S21. Cell viability of NIH 3T3 mouse fibroblasts encapsulated in crosslinked **DN1-6** hydrogels for 24 h. Mean ± SD, N ≥ 3.

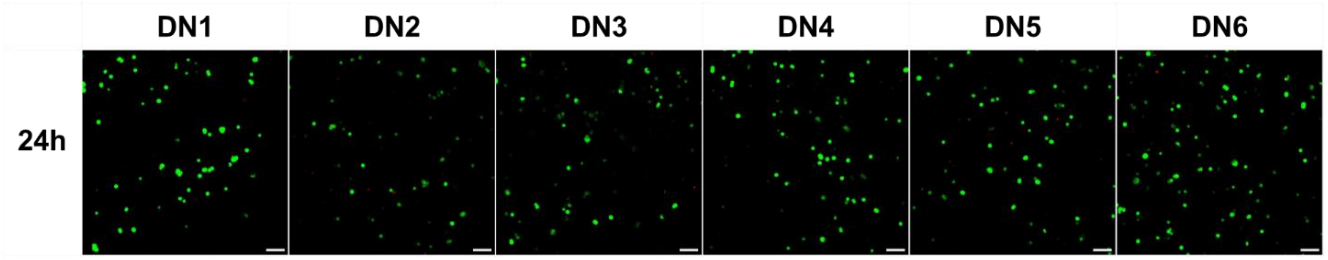

Figure S22. Confocal microscopy images of N3T3 cells encapsulated in crosslinked **DN1-6** hydrogels for 24 h. Calcein AM (green) and propidium iodide (red) mark the live and dead cells, respectively. Scale bar: *200 µm*.

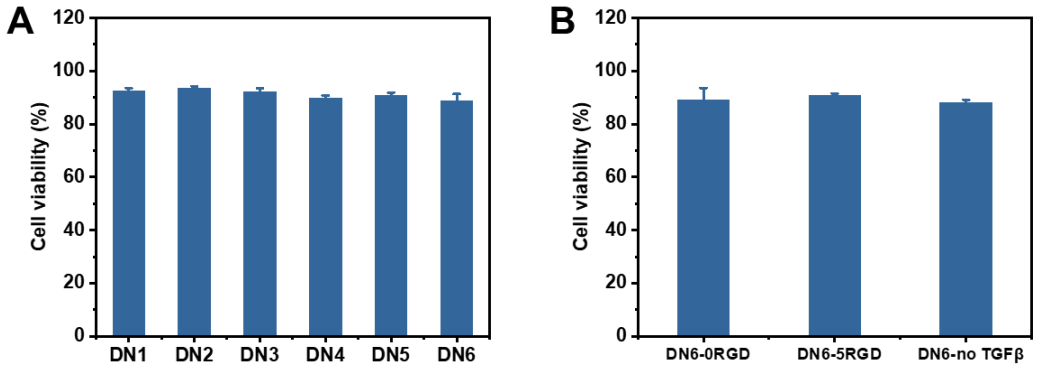

Figure S23. Cell viability of hPACs encapsulated in crosslinked (A) **DN1-6** hydrogels with 10 mol% SQ-RGD and (B) **DN6-5%RGD, DN6-0%RGD** and **DN6-no TGFβ** hydrogels for 24 h. Mean ± SD, N = 3. All cell-laden hydrogels were maintained in chondrogenic media containing TGF-β1 except for **DN6-no TGFβ** hydrogel.

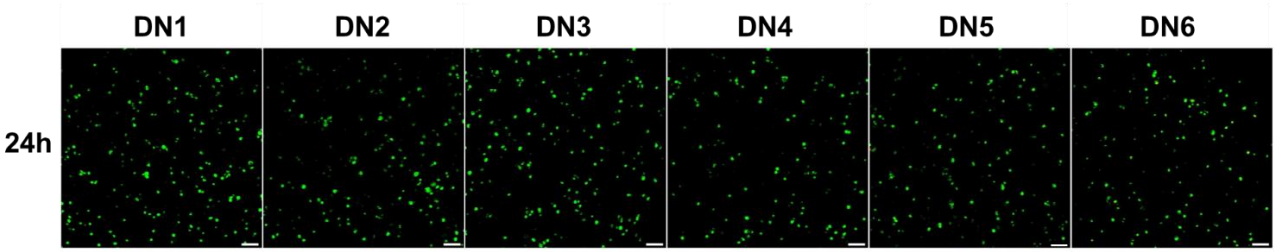

Figure S24. Confocal microscopy images of hPACs encapsulated in crosslinked **DN1-6** hydrogels with 10 mol% SQ-RGD for 24 h. Calcein AM (green) and propidium iodide (red) mark the live and dead cells, respectively. All cell-laden hydrogels were maintained in chondrogenic media containing TGF-β1.

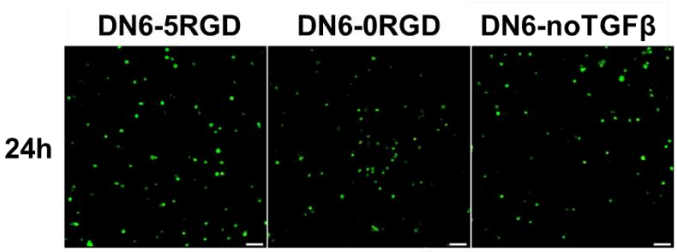

Figure S25. Confocal microscopy images of hPACs encapsulated in crosslinked **DN6-5%RGD, DN6-0%RGD** and **DN6-no TGFβ** hydrogels for 24 h. Calcein AM (green) and propidium iodide (red) mark the live and dead cells, respectively. All cell-laden hydrogels were maintained in chondrogenic media containing TGF-β1 except for **DN6-no TGFβ** hydrogel.

Mechanical loading experiment

Agarose culture wells with a diameter of 4 mm and a height of 1 mm were prepared by putting agarose (350 µL, 3%) in each well of a 24-well flat-bottom plate, using a 4 mm metal punch to create a small hole in the middle of the solidified agarose. The cell-laden hydrogel **DN** (20 µL) before photocrosslinking was gently pipetted into agarose wells. Then the hydrogels were exposed (2 min) to visible light using a benchtop LED. Chondrogenic differentiation media (500 µL) with TGF-β1 (10 ng/ml) was carefully pipetted on top of the construct. The plate was cultured under standard cell culture

conditions. Cell media was refreshed 3 times every 15 min after seeding and was changed daily during the experiment.

For short-term (2 days) loading, the cell culture medium was carefully removed from the culture plate and the hydrogels were washed once with PBS and then covered with PBS. Mechanical loading was performed continuously using cycles consisting of 10 min periods with 2% strain amplitude at the fixed frequency of 1.0 Hz at RT using the MACH-1 machine. After loading, the constructs were covered with chondrogenic differentiation media (500 µL) and further cultured under standard conditions. The control constructs were placed in the RT for 10 min with PBS and without subjecting the mechanical loading.

Alcian Blue staining

To perform Alcian Blue staining for sulfated glycosaminoglycans (s-GAGs), the hydrogel encapsulated hPACs were first fixed with 4% formaldehyde at RT for 20 min. The constructs were washed PBS (3 x 500 µL) and incubated with HCl (0.1N, 500 µL) for 10 min at RT. To detect s-GAGs, constructs were Alcian Blue 8-GX (1%) in HCl (0.1N) for 3 h and with HCl (0.1N, 3 x 500 µL), followed by adding HCl (0.1N, 500 µL) and incubated at RT overnight to remove the excess Alcian Blue. The constructs were washed with Milli-Q water (3 x 500 µL) before adding nuclear fast red (0.1% in 5% aluminum sulfate) to stain the cell nuclei and incubated for 10 min before washing with MilliQ water (3 x 500 µL) before imaging.

DMMB assay and DNA content analysis

The s-GAGs and DNA content at different time points were quantified using biochemical analysis. The wet cell-hydrogel constructs were first weighed and digested overnight at 60 °C with a papain digestion solution in PBS-EDTA (pH 7.1). The s-GAGs concentration was measured in a medium collected at pre-determined time points from the hydrogels. s-GAGs content of the digested samples was quantified using a dimethylmethylene blue (DMMB) assay, with shark chondroitin sulfate in PBS-EDTA (pH 7.1) as a reference. The collected medium from the chondrogenic compartment was diluted 30x before performing a DMMB staining measuring absorbance at 525 and 595 nm. The concentrations of DNA from the digested hydrogel samples were directly measured on a nanodrop.

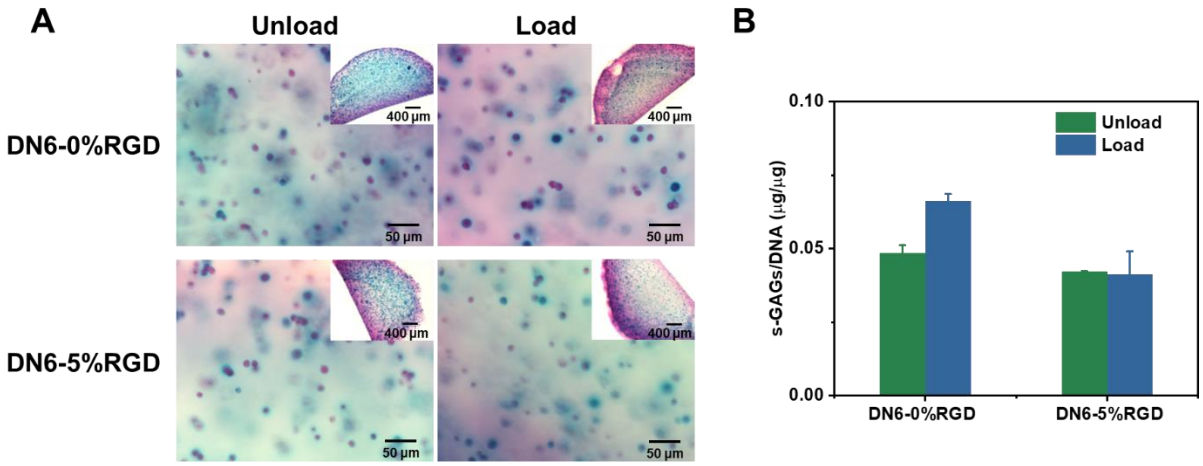

Figure S26. (A) Alcian Blue staining of s-GAGs with nuclear fast red counterstaining of hPACs in cell-laden **DN6-5%RGD, DN6-0%RGD** after 2 days culture or soft loading. (B) Results of biochemical analysis of s-GAGs deposition relative to DNA content in **DN6-5%RGD, DN6-0%RGD** after 2 days culture or soft loading. All the cell-laden hydrogels were maintained in chondrogenic media containing TGF-β1.

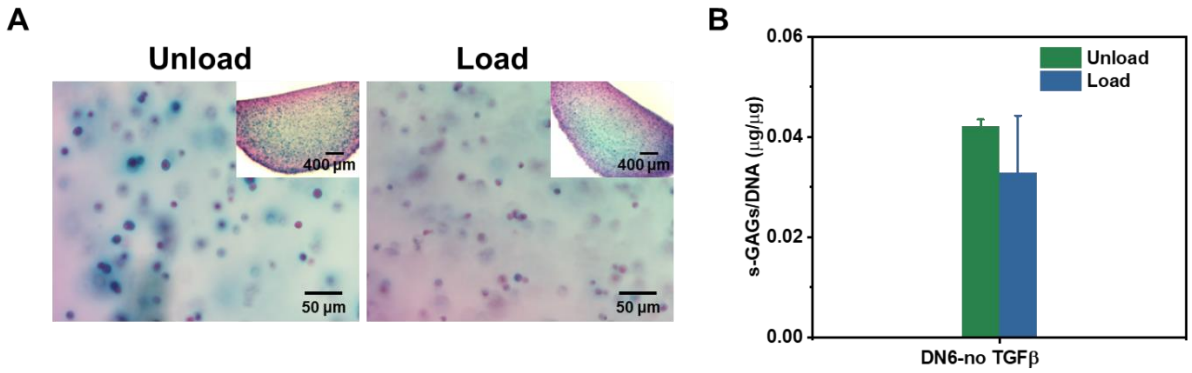

Figure S27. (A) Alcian Blue staining of s-GAGs with nuclear fast red counterstaining of hPACs in crosslinked **DN6-no TGFβ** hydrogels after 2 days culture or soft loading. (B) Results of biochemical analysis of s-GAG deposition relative to DNA content in crosslinked **DN6-no TGFβ** hydrogels after 2 days of culture or soft loading. All the cell-laden hydrogels were maintained in chondrogenic media without TGF-β1.

Reference

(1) Lengyel, G. A.; Horne, W. S. Design strategies for the sequence-based mimicry of side-chain display in protein β-sheets by α/β-peptides. Journal of the American Chemical Society 2012, 134 (38), 15906.

(2) Tong, C.; Wondergem, J. A. J.; van den Brink, M.; Kwakernaak, M. C.; Chen, Y.; Hendrix, M.; Voets, I. K.; Danen, E. H. J.; Le Devedec, S.; Heinrich, D.et al. Spatial and Temporal Modulation of Cell Instructive Cues in a Filamentous Supramolecular Biomaterial. ACS Appl. Mater. Interfaces 2022, 14 (15), 17042.

(3) Chan, E. P.; Deeyaa, B.; Johnson, P. M.; Stafford, C. M. Poroelastic relaxation of polymer-loaded hydrogels. Soft Matter 2012, 8 (31), 8234.

(4) Soltanahmadi, S.; Raske, N.; de Boer, G. N.; Neville, A.; Hewson, R. W.; Bryant, M. G. Fabrication of Cartilage-Inspired Hydrogel/Entangled Polymer–Elastomer Structures Possessing Poro-Elastic Properties. ACS Applied Polymer Materials 2021, 3 (5), 2694.

(5) Bomer, N.; den Hollander, W.; Ramos, Y. F.; Bos, S. D.; van der Breggen, R.; Lakenberg, N.; Pepers, B. A.; van Eeden, A. E.; Darvishan, A.; Tobi, E. W.et al. Underlying molecular mechanisms of DIO2 susceptibility in symptomatic osteoarthritis. Ann Rheum Dis 2015, 74 (8), 1571.